THESIS

A NOVEL METHODOLOGY FOR THE RESILIENCE ASSESSMENT OF ELECTRIFIED ROAD TRANSPORTATION SYSTEMS

Submitted by
Felix Kuklinski
Department of Systems Engineering

In partial fulfillment of the requirements
For the Degree of Master of Science
Colorado State University
Fort Collins, Colorado
Spring 2026

Master's Committee:

Advisor: Thomas Bradley

Erika Gallegos
John van de Lindt

ABSTRACT

A NOVEL METHODOLOGY FOR THE RESILIENCE ASSESSMENT OF ELECTRIFIED ROAD TRANSPORTATION SYSTEMS

Progression of climate change causes increased exposure of transportation infrastructure to natural hazards. Subsequent decarbonization efforts such as the shift to electric vehicles (EVs) introduce new operational dependencies, which can adversely affect the functionality of road transportation following disruptions. These trends motivate the need for methods to characterize and quantify resilience of electrified transportation systems. This thesis develops a two-stage modeling framework that quantifies resilience using three performance dimensions: travel delays, charging delays and queueing delays. In the first stage a novel traffic assignment model with an integrated energy model and range constraints is formulated to yield equilibrium travel delays and charging demands. In the second stage, these charging demands are used in a Monte Carlo simulation of charging station locations to estimate charging and queueing delays. This methodology was applied to two case study scenarios of Northern Colorado with the prolonged closure of a major roadway, based on conditions during the Cameron Peak wildfire. At 4.52% EV ownership rate, results indicate that the overall performance degradation experienced by EVs is strongly contingent on high-power high-capacity charging facilities remaining operational in the disrupted region. For further analysis disaggregated resilience results inform interventions, which are modeled and evaluated to provide decision support. These findings support the use of disaggregated resilience metrics and the proposed assessment methodology for the identification and evaluation of targeted interventions to mitigate bottlenecks and improve electrified transportation system resilience.

ACKNOWLEDGEMENTS

This material is based upon work supported by the Joint Office of Energy and Transportation through the U.S. Department of Energy's Office of Energy Efficiency and Renewable Energy (EERE) under Award Number DE-EE0011232.

TABLE OF CONTENTS

1. Introduction

Transportation systems represent an important element of a functioning society. They facilitate the transport of goods and services and enable personal mobility [1]; but the performance of the transportation system can be degraded under environmental or human-induced disruptions. Making a system entirely resistant to these hazards, particularly one as diverse and expansive as transportation would be extraordinarily costly. Instead, the concepts of resilience provide a means to quantify and improve the performance of transportation systems before, during and after disruption [2]. Resilience concepts include resistance to functionality loss following a disruption but also emphasize the timeliness of recovery [3]. In the domain of transportation engineering, resilience enhancements have been shown to yield high economic and functional returns, relative to cost of repairs or reconstruction [4], [5]. The interest in resilient transportation infrastructure has increased due to growing exposure of infrastructure to environmental hazards from climate change and other stressors [6], [7].

In the past decade electric vehicles (EVs) have emerged as a new technology to be integrated into the transportation sector. Road transport using EVs, however, presents particular resilience challenges, due to its reliance on the networked function of a diverse set of supporting systems, including a high-power electricity grid system, telecommunication system, the road network system, maintenance systems, and more. Electrified transportation infrastructure is, therefore, perhaps particularly vulnerable to prolonged loss of functionality under resilience stressors, which will carry implications for performance of the transportation system as a whole, as the importance and adoption of electrified transportation increases.

EVs have been the subject of transportation system resilience research, which generally finds that EVs have measurable resilience challenges in concepts. EVs have a characteristically slower "refueling" (or recharging) rate than internal combustion engine vehicles (ICEVs), which along with fewer charging stations than gasoline/diesel refueling stations can lead to large increases in queueing times [8] from increases in demand. The reduced geographical coverage of EV charging stations, compared to petroleum stations, may necessitate detours and delays in transportation system function.

These issues disproportionately affect rural areas and underserved communities, due to the quality and insufficient availability of enabling systems, as well as a lack of capital investment. Such communities are typically located in areas with greater exposure to natural hazards [9], [10], warranting special attention when considering equitable accessibility to electrified transport.

1.1. Resilience Definition

The term resilience first appeared in a systemic context in the field of ecology, where it was used to describe an ecosystem's capability to retain stability when subjected to changes and disturbances, or to rapidly return to an equilibrium state [11]. It was later adopted within numerous other domains, including engineering. Engineering resilience describes a system's capabilities to maintain functionality, lose functionality "gracefully", and rapidly return to the original or an improved system state [12], [13].

1.1.1. Infrastructure and Transportation Resilience

Resilience can be characterized in a number of ways, and examples from the literature are relevant to the discussion. In the context of earthquake engineering, Bruneau et al. [14] define community seismic resilience as "the ability of social units (e.g., organizations, communities) to mitigate hazards, contain the effects of disasters when they occur, and carry out recovery activities in ways that minimize social disruption and mitigate the effects of future earthquakes". Four dimensions – Technical, Organizational, Social, Economic (TOSE) – that shape a community's ability to withstand and recover from earthquakes are described. Technical resilience can be further disaggregated into four components, the four R's – Robustness, Redundancy, Resourcefulness and Rapidity, which are widely recognized as ways to characterize resilience [15], [16], [17], [18]. Robustness considers the extent to which a system can be stressed without exhibiting a loss of performance; Redundancy describes the number of alternative resources a system provides that facilitate comparable performance; Resourcefulness is a system's capability to identify problems, establish priorities, and mobilize resources (e.g., human, or monetary resources) to mitigate system disruption; and, Rapidity describes the rate at which system performance is recovered.

Robustness and Rapidity are the explicit performance characteristics of the system ("ends"), whereas Resourcefulness and Redundancy are their enabling characteristics ("means"). These "means" represent the resources invested into a system to facilitate its performance, either through maintaining or recovering functionality.

Key to this work is the concept of a resilience triangle. It represents a way to quantify resilience as the total, relative loss of functionality over time. This is shown in Figure 1, where the y-axis shows the relative performance of the system, given in percent at time t, through the quality function, $Q(t)$. The resilience triangle gets its name from the linear interpolation of the dynamic relative performance of a system, as shown in Fig. 1. The height of the triangle then shows the severity of performance loss. Robustness and Rapidity can be described using the resilience triangle, where robustness is the remaining functionality of a system after the disruption [19] and rapidity is the length of the triangle, showing the total time and characteristics of the system's recovery [14]. The associated metric presented on this basis is Eq. (1) (also taken from [14]):

$$L = \int_{t_0}^{t_1} [100 - Q(t)]\, dt, \tag{1}$$

where t_0 is the time right before the disruption manifests, and t_1 is the time at which the system recovers full functionality. It calculates the area of lost performance relative to the baseline level at t_0.

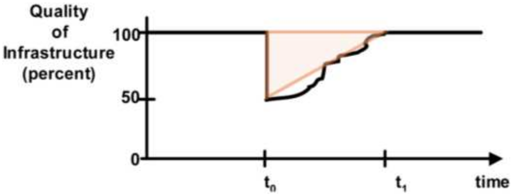

Figure 1 Relative system performance over time during a disruptive event (modified from [14])

The work of Bruneau et al. [14] has been adopted and expanded to additional disciplines by other authors. Chang and Shinozuka [20], for example, develop a probabilistic metric for quantifying system functionality, based on standards for robustness and rapidity. These are evaluated by comparing baseline and disrupted conditions and applied to a case study of the water system of Memphis, TN. Cimellaro et al. [21] build on the TOSE resilience dimensions to develop the PEOPLES framework, which quantifies community resilience by determining an index that considers the following dimensions: Population and demographics; environment and ecosystem; organized government service; physical infrastructure; lifestyle and community competence; economic development; and social-cultural capital.

Also based on the framework presented in [14], Reed et al. [22] develop an approach for the assessment of resilience of networked infrastructure. They use fragility and quality as metrics of performance and create an interdependency matrix based on Leontief's input-output model to assess the interoperability of various infrastructures for hurricanes and seismic events. To quantify resilience, they build on the resilience triangle concept (described above), by normalizing the relative performance function to define the resilience index as:

$$R = \frac{\int_{t_0}^{t_1} Q(t)\, dt}{t_1 - t_0}. \tag{2}$$

Eq. (2) yields a mean performance retained over the simulated duration and serves as the basis for the resilience metrics developed in the present study.

Numerous methods for measuring transportation resilience have been proposed. Previous studies have employed graph theoretical methods and metrics [1], [23], [24], [25], probabilistic methods [26], fuzzy-logic approaches [27], [28], simulation models [13], and optimization models [29], [30].

Measures of resilience can be grouped into topological, attribute-based, and performance metrics [19]. The latter category measures system functionality based on its intended purpose. One frequently utilized performance metric, for instance, is the expected demand satisfied by the system under disruption relative to its baseline [26], [31]. Alternatively, several authors have leveraged optimization models in the form of traffic assignment problems (TAP) to derive travel times as a functionality metric [18], [29], [32]. The use of system performance metrics as a basis for resilience quantification enables the capture of system behavior in a comprehensive way. Attribute-based metrics, on the other hand, quantify only the specific contributors to a resilient system (e.g. robustness, rapidity) [19]. This thesis defines resilience as the mean retained performance across discrete steady-state system states, rather than modeling continuous system dynamics.

1.1.2. EV Infrastructure resilience

Given the compounding challenges electrified transport is faced with, recent research has begun extending resilience concepts to this domain. While transportation system resilience has been widely studied, the body of research addressing the resilience of EV road transport remains comparatively limited.

Zhang et al. [33] developed a multi-objective optimization (MOO) program for the resilient location of charging infrastructure in flood-prone areas by integrating a flood impact model. To this end, customer satisfaction is maximized, flood impact is minimized and distance between charging stations is maximized. Customer satisfaction, or charging willingness, is characterized by the dwell time at the charging location and its distance from the destination. The authors utilize a non-dominant sorting genetic algorithm-III (NSGA-III) to solve the MOO problem, after which the technique for order of preference by similarity to ideal solution (TOPSIS) is proposed to determine the best solution out of the feasible candidates. This framework was applied to a case study of the Waikiki area in Oahu, HW for a short- and long-term planning scenario with respect to sea-level rises.

Hussain et al. [34] proposed an MOO program for optimally supplying electricity to EVs during a power outage to enable critical transport functions despite system disruptions. This program distributed constrained energy resources such that customer satisfaction is maximized, first prioritizing societal, then community, and last, individual satisfaction. The program is solved using five different techniques, comparing the results using the demand and total demand fulfillment indexes. These represent the fraction of EVs whose charging demands were satisfied for each priority level and the system as a whole, respectively.

Raman et al. [35] conducted data-driven case study of the charging station resilience of the Greater London area to urban flooding. The authors simulated EV trips based on vehicle driving pattern data to evaluate the usage of the charging stations in the area at a baseline and flooded state with three different intensities. To assess the network, charger utilization and the distance between charging stations and trip destinations are proposed. Additionally, based on the first results, the authors suggest strategies for placing charging stations to alleviate overutilization and improve accessibility.

Hamim et al. [36] propose a framework for the resilience assessment of EV charging station networks. To this end, a Voronoi graph of the EV charging infrastructure network is created, where Voronoi diagrams are weighted on the attractiveness potential of the corresponding charging stations, based on output power, daily trips per person, the number of visits to commercial points of interest, and EV penetration. The centroids are then shifted in their respective polygons according to their relative attractiveness to adjacent centroids. The authors represent network performance using betweenness centrality and graph efficiency. They then apply this framework to 12 U.S. states and characterize their EV charging station network resilience by progressively removing targeted and random nodes while observing network performance.

Finally, Wang et al. [37] develop a framework to study the resilience of road networks to fast charging station failures. To this end, a cell transmission model was extended to develop a dynamic traffic assignment model. Wang et al [37] further propose an index-based metric for system-level resilience, using the number of EVs completing their trip as a performance function. At a component-level they define the cumulative utilization metric that quantifies each charging station’s contribution to the total energy delivered to EVs over the studied period. This framework was applied to a benchmark network under different combinations of charging stations failures, failure durations, and locations.

Our review of the literature suggests that the resilience of electrified road transportation is proportionally understudied, despite the challenges it faces. Existing research primarily quantifies EV transportation resilience at a charging station-level [35], [36], [37], often neglecting the effects that necessary detours and knock-on effects on surrounding traffic have on system-level performance.

1.2. Contributions

To fill the gaps noted above, this thesis contributes to the body of literature on resilience assessment for EVs in three ways. First, it develops a two-class queueing-agnostic EV user equilibrium traffic assignment problem (TAP), that incorporates energy-based range constraints through stochastic state-of-charge (SOC) distributions. Second, it provides steady-state estimates for queueing and charging delays at charging locations with heterogeneous electric vehicle supply equipment (EVSE), by coupling traffic assignment results with a Monte Carlo simulation of charging stations. Third, it develops a set of disaggregated performance-based resilience metrics, that extend the resilience index of Reed et al. [22] along three dimensions - travel, charging, and queueing delays. This enables component-level diagnosis of performance degradation to provide actionable identification of bottlenecks. Together, these contributions provide a unified methodology for the quantification of resilience of energy-constrained electrified transport.

2. Electrified Transportation System Performance Assessment Framework

To assess the resilience of an electrified transport system, the set of system-level performance losses relevant to electrified transportation - travel delays, charging delays, and queueing delays - must be determined. To this end, the proposed framework evaluates individual performance dimensions by integrating energy-constrained route choice behavior with stochastically distributed starting SOCs and simulations of charging station operations within a unified architecture (illustrated in Fig. 2). The simulation consists of three modules: (i) Feature extraction from transportation system and EV user base data, (ii) a static traffic assignment (STA) model with stochastic range constraints, and (iii) a Monte Carlo simulation of charging station operations. Together these modules enable a steady-state performance assessment of the electrified transportation system. This framework is executed for a baseline and one or more disrupted system states, and the resulting performance measures serve as the basis for computing resilience metrics (defined in Section 5).

First, the simulation (illustrated in Fig. 2) begins with a feature extraction stage which synthesizes and appropriately parameterizes a detailed traffic and charging network model within the spatial boundaries of the analyzed region. Charging station data is aggregated into charging station locations and assigned to network links, their expected output powers are estimated, and EV ownership fraction within each traffic analysis zone (TAZ) are specified. The spatial aggregation of TAZs serves as the basis for analysis. Origin-destination (OD) trip data is aggregated and assigned to the centroid representing TAZs. Each OD matrix value, then, represents the steady-state travel demand $\left[\frac{veh}{h}\right]$ between centroids that correspond to its row and column indices. The framework, thus, yields steady-state outputs for each system state, where the TAP produces equilibrium path flow rates. The temporal scope of a simulation is defined by a set of discrete system states of specific durations, $\{T_1, \ldots, T_n\}$, each with constant demand, topology, and charging infrastructure, producing a set of steady-state performance measures. The proposed TAP distinguishes between two vehicle classes: non-recharging vehicles (ICEVs and high SOC EVs) and recharging vehicles (EVs with SOCs inadequate to reach their destination). The OD matrix is vehicle class-agnostic. Path sets are then created to connect each OD-pair in the matrix that includes shortest paths through the unloaded network. For recharging EVs, these take into account the distance of charging stations using deterministic OD-pair travel distances and probabilistic SOC distributions (see Section 3.2.5). These initial path sets serve as the basis for justification of trip feasibility and vehicle classification (into recharging or not recharging EVs). Infeasible shortest paths determine the EV travel demand that cannot be satisfied due to insufficient SOC, which enables the creation of vehicle class-specific OD matrices.

The second module (illustrated in Fig. 2) solves the two-class traffic assignment problem using as inputs the feature extraction output data to output path flows that are congruent with the range restrictions imposed by origin-specific starting SOC distributions. This TAP is solved using a using MATLAB's interior-point optimizer for constrained nonlinear optimization programs (NLP). The collection of path flows, then, enables the calculation of travel delays for each trip to represent the first performance dimension necessary for resilience assessment.

Lastly, the integration of energy demands with path flows enables a stochastic simulation of charging station function. The flow of vehicles into each charging station location, and their respective energy demands, are used as inputs to a Monte Carlo simulation that provides a simulation of charging behavior at each EVSE, yielding steady-state, path-specific estimates of mean queueing duration and charging duration for each travel path. These constitute the remaining two performance dimensions utilized in this study's resilience assessment of electrified transportation systems.

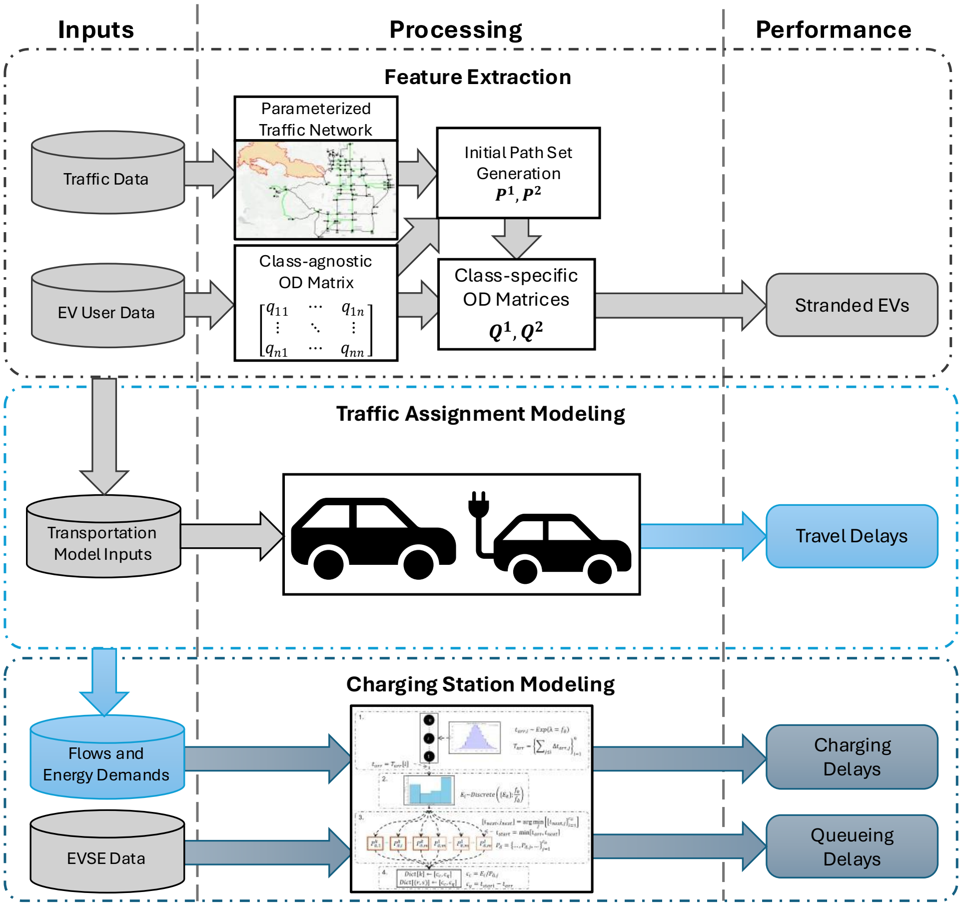

Figure 2 Proposed framework for performance assessment of electrified transportation systems

3. Traffic Assignment Model

To simulate the electrified transportation system's functional performance, a novel two-class static traffic assignment (STA) problem formulation is proposed. STA models have been widely used for the assessment of transportation system resilience [17], [18], [29], [30], due to their ease of customization, lower computational cost compared to dynamic and simulation-based models. They are particularly pertinent to resilience assessment where the duration of system disruptions are long relative to traffic transients and where the spatial scope of the transportation system is large. The STA formulation proposed here is novel in that it links vehicle SOC modeling with range-constrained path flows and provides integration with charging location-level simulation. The integrated energy model enables modeling of a variety of scenarios and their effects on system, and thereby, model parameters.

3.1. Behavioral Assumptions

There is a large body of research modeling the behavior of alternate fuel vehicles requiring enroute refueling [38]. This material has been adapted to EVs for the purpose of optimal charging station location [39], [40], [41] and load forecasting on the power grid [42]. To accurately represent charging station selection and associated network flows, the traveler behavior must be modeled. The charging pyramid, a commonly applied model for the frequency of charger usage, postulates that owners prefer recharging their EV during long dwell time (e.g., home, at work) [43]. Since the use of public chargers necessitates an extraneous time investment, EV travelers only choose to visit them if their desired trip cannot otherwise be completed. In accordance with Wardrop's first principle [44], should an EV user need to refuel enroute, the charging station location is chosen such that the lowest (value-of-time adjusted) cumulative commute time is achieved [45]. This choice is not just dependent on the expected charging rate, but also the energy that one must recharge. Additional factors such as amenities and cost of charging [46] are commonly found to impact charging decisions. However, to maintain comparability between scenarios where minimizing delays may be significantly favored due to the nature of the disruption, these factors are not considered.

Other authors include queueing delays as a factor in the path choice of recharging EVs [47], [48]. However, the congestion and associated queueing time at charging stations is invisible to travelers as they plan their route. Furthermore, most EV owners select their charging station location ahead of time, and without consideration for queueing [46]. The choice of charging station is, therefore, influenced by its expected output power, its proximity to the origin, the length of detour required to reach it, and the EV's starting SOC.

Therefore, to model the reachability of charging stations from a given origin and the energy required to recharge an EV to its target SOC, an energy model is implemented that stochastically distributes the starting SOCs of EVs departing from a given node. This distribution enables (i) the calculation of a path-specific mean total energy required at a charging station and (ii) stochastic path constraints based on the proximity of a given path's charging station to the origin (i.e., only the fraction of EVs that can reach a path's charging station can take that path). This permits the modeling of detours to reach charging stations, modeling of charging delays from having to use lower power charging stations, and modeling of resulting queueing times. For this study, the feasible paths for enroute charging EVs are limited to a single recharging stop, with each vehicle that stops at a charger always charging their battery to 80% of their maximum SOC [49] (as in [8], [35]). Non-recharging vehicles are not subject to any path-choice constraints.

3.2. Mathematical Formulation

3.2.1. Network Topology and Vehicle Class definition

The topology and traveler class distinction presented in [47] are adopted in this study. A two-class traffic assignment model is proposed, where it is differentiated between the travelers that must visit a charging station enroute (RV) ($m = 2$), and those that do not recharge their vehicles (NRV) ($m = 1$). The latter class constraints both ICEVs and EVs with sufficient charge to complete their trip.

Consider a directed graph $G(N, A)$ composed of a set of nodes N and directed links $a \in A$, where nodes represent sources and destinations of travel demand from TAZs and intersections and links represent roadways. Charging stations are represented in the network through secondary links $\tilde{a} \in \tilde{A}$ that run in parallel to the roadways on which they are situated, such that $\tilde{A} \subseteq A$. This allows for the aggregation of charging stations along a road segment. To illustrate the topology, consider Figure 3, which shows a simple network graph with 4 nodes connected in series. The road segment between nodes 2 and 3 has a set of charging stations assigned to it. Therefore, a secondary charging station link, $\tilde{a}_1$, is present.

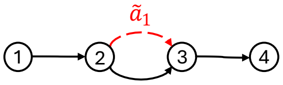

Figure 3 Example network graph of topology convention

Nodes in the network graph serve as the sources $r \in N$ and destinations $s \in N$ of traffic. An OD-pair $(r, s) \in W$, then, describes the combination of nodes between which a traffic demand $q^{rs} \in Q^{rs}$ exists. This traffic demand represents the overall, vehicle class-independent trip demand between two nodes in the network. Based on the EV-penetration, γ^r, and energy distribution at the origin node $r \in N$, Q^{rs} can be disaggregated for the vehicle classes $m \in M = \{1,2\}$. Their trip demands between an OD-pair $(r, s) \in W$ are then $q^{1,rs}$ and $q^{2,rs}$, respectively.

This class-specific demand must be allotted to paths $k \in P^{m,rs}$, which is a sequence of links $a \in A$ connecting the nodes of a given OD-pair $(r, s) \in W$. Vehicles that recharge must do so at charging stations. Therefore, their paths $k \in P^{2,rs}$ must contain one, and only one, secondary charging station link $\tilde{a} \in \tilde{A}$. Conversely, because NRVs do not recharge enroute, their paths $k \in P^{1,rs}$ must not contain secondary links. A link-path incidence matrix Δ^m defines the composition of paths using binary elements $\delta_{a,k}^{m,rs}$, where $\delta_{a,k}^{m,rs} = 1$ if $a \in k$ connecting the OD-pair $(r, s) \in W$ in vehicle class $m \in M$ and otherwise $\delta_{a,k}^{m,rs} = 0$.

The traffic assignment yields traffic flows $f_k^{m,rs}$ of vehicle class $m \in M$ on path $k \in P^{m,rs}$. Since TAPs seek to allocate demands between OD-pairs to paths connecting them, the sum of all flows for a given class $m \in M$ between each OD-pair must result in the demand:

$$\sum_{k \in P^{m,rs}} f_k^{m,rs} = q^{m,rs} \,, \qquad \forall m \in M, (r,s) \in W. \tag{3}$$

Clearly,

$$f_k^{rs} \geq 0, \qquad \forall k \in P^{m,rs}, m \in M, (r,s) \in W. \tag{4}$$

The flow on individual links x_a of the network, then, is the sum of all path flows using that link, given in Eq. (5):

$$x_a = \sum_{m \in M} \sum_{(r,s) \in W} \sum_{k \in P^{m,rs}} f_k^{m,rs} \delta_{a,k}^{m,rs} \,. \tag{5}$$

3.2.2. Travel delays

The travel time experienced by road segment users, c_a, is dependent on the vehicle flow x_a on a given road segment $a \in A$. The formulation for this thesis applies the widely used Bureau of Public Roads (BPR) travel time function defined as:

$$c_a(x_a) = t_{0,a} \left(1 + \alpha_a \left(\frac{x_a}{Q_a} \right)^{\beta_a} \right), \tag{6}$$

where $t_{0,a}$ [h] is the free flow travel time on link $a \in A$, Q_a is a link's road capacity $\left[\frac{veh}{h}\right]$, and α_a and β_a are link-specific parameters that characterize their congestion behavior on a given road segment. The flow on a given road segment is the cumulative flow of all paths, regardless of vehicle class and to accurately represent the travel delays between two nodes connected by a primary and charging station link, their cumulative flow must be used in Eq. (6).

3.2.3. Energy Model

The energy demand (in kWh), E_k^{rs}, of a set of EVs departing from origin node $r \in N$ using the path $k \in P^{2,rs}$, which uses the charging station $\tilde{a} \in \tilde{A}$, is computed as:

$$E_k^{rs} = E^r + E_k^{r\tilde{a}}, \tag{7}$$

where E^r is the starting energy demand and $E_k^{r\tilde{a}}$ is the energy required to travel from the origin node $r \in N$ to the charging station link $\tilde{a} \in \tilde{A}$. It represents the total energy that EVs, using path $k \in P^{2,rs}$, require to recharge their battery.

The starting energy demand is determined from the node-specific starting energy distribution, which is defined as:

$$f^r(x; \alpha, \beta) \sim Beta(\alpha^r, \beta^r). \tag{8}$$

Eq. (8) represents a Beta distribution that reflects the starting SOCs [%] of EVs departing from the origin node $r \in N$, and is characterized by the shape parameters α^r and β^r. The charging energy required for EVs to complete their trip can be computed as:

$$E^r = E_{max}(1 - \mathbb{E}[f^r(x; \alpha, \beta)]) = E_{max}\left(1 - \frac{\alpha^r}{\alpha^r + \beta^r}\right), \tag{9}$$

where E_{max} represents a singular value of the useful battery capacity (80% of the total capacity) of the model of EVs in the transportation network $[kWh]$.[1]

The energy expended during travel between the origin node $r \in N$ and the path's charging station link $\tilde{a} \in \tilde{A}$ is calculated with:

---

[1] Only one "make and model" of EV is assumed to make up the entire fleet of EVs in this study. Distributions of EV battery capacity and energy consumption are admissible inputs to this model

$$E_{k,t}^{r\tilde{a}} = u\left(\sum_{i=1}^{\tilde{a}-1} d_{k,i} + \frac{d_{k,\tilde{a}}}{2}\right), \tag{10}$$

where $d_{k,i}$ is the length of the i-th link $[km]$ on path k, and u represents the globally constant parameter for the energy consumption of EVs $\left[\frac{kWh}{km}\right]$. $\frac{d_{k,\tilde{a}}}{2}$ represents half the length of the charging station link used in path k, which enables the modeling of bidirectional access to a charging station location along a given road segment.

The resulting expected delay, $c_{k,\tilde{a}}^{2}$, is dependent on the assumption around which SOC is sufficient for travelers to end the charge cycle:

$$c_{k,\tilde{a}}^{2} = \eta \frac{E_{k}^{rs}}{\bar{P}_{\tilde{a}}}, \tag{11}$$

where $\bar{P}_{\tilde{a}}$ is the expected charging power $\left[\frac{kWh}{h}\right]$ at a charging station location, and η is a unitless scaling factor for the value of time (VOT), while waiting for the car to recharge, relative to the VOT during active travel. It scales charging delays, converting them to a generalized cost that enables direct comparison to travel delays. It is noted here that the modeled route choice behavior is based on the assumption that EV operators recharge their vehicles to 80% SOC at each charging stop.[2]

3.2.4. Vehicle Class Travel Demand

Because travel of EVs is energy constrained, the following equations describe the vehicle-class-specific travel demands:

$$q^{2,rs} = q^{rs}\gamma^{r} F\left(\frac{E_{min}^{rs}}{E_{max}};\ \alpha^{r}, \beta^{r}\right) - q_{stranded}^{rs} \tag{12a}$$

---

[2] This behavior can be easily modified by adjusting Eq. (7) such that the minimal amount of energy to complete the trip is recharged

$$q_{str}^{rs} = q^{rs}\gamma^{r}F\left(\frac{E_{\tilde{a},1}^{rs}}{E_{max}};\ \alpha^{r},\beta^{r}\right) \tag{12b}$$

$$q^{1,rs} = q^{r} - q^{2,rs} - q_{stranded}^{rs} \tag{12c}$$

where E_{min}^{rs} describes the energy required for completing the shortest path $[kWh]$ between an OD-pair $(r,s) \in W$, q^{rs} is the total travel demand between OD-pair $(r,s) \in W$, and γ^{r} is the fraction of EVs in the vehicle population (EV penetration) of node $r \in N$. To reiterate, $q^{1,rs}$ and $q^{2,rs}$ represent the travel demands for the given OD-pair of vehicle types $m = 1$ and $m = 2$ respectively. q_{str}^{rs} represents the number of EVs that intend to travel between OD-pair $(r,s) \in W$, but are unable to start their trip $\left[\frac{veh}{h}\right]$ due to insufficient SOC to reach the closest charging station and are therefore stranded. $F(\cdot)$ is the cumulative distribution function corresponding to the SOC distribution in Eq. (8). Here, $E_{\tilde{a},1}^{rs}$ represents the energy required to reach the charging station using the feasible path with the smallest distance between origin node $r \in N$ and the charging station link $\tilde{a} \in \tilde{A}$. Individual travel demands for every OD-pair $(r,s) \in W$ are stored in OD matrices, where the total travel demand OD matrix is denoted $\boldsymbol{Q}$ and vehicle-class-specific OD-matrices are denoted $\boldsymbol{Q^{1}}$ and $\boldsymbol{Q^{2}}$, respectively.

3.2.5. Range Constraints

The range restriction imposes further path flow constraints on charging EVs, because the distance of a charging station from the origin of a certain path $h \in P^{2,rs}$ may be too far for a fraction of EVs to travel. Therefore:

$$\sum_{i \in \mathcal{E}_{h}} f_{i}^{2,rs} \leq U_{h}^{2,rs}, \qquad \forall h \in P^{2,rs}, (r,s) \in W, \tag{13}$$

$$U_{i}^{2,rs} = q^{2,rs}\left[1 - F_{T}\left(\frac{E_{i,t}^{r\tilde{a}}}{E_{max}};\alpha^{r},\beta^{r}\right)\right], \tag{14}$$

where $F_T\left(\frac{E_{k,t}^{r\tilde{a}}}{E_{max}};\alpha^r,\beta^r\right)$ computes the fraction of EVs that is unable to reach the charging station. $F_T(\cdot)$, then, is a truncated cdf of the pdf in Eq. (8), having limits between the minimum SOC required to reach the closest charging station $\frac{E_{\tilde{a},1}^{rs}}{E_{max}}$ and the SOC required to traverse the shortest-distance path E_0 between the OD-pair $(r,s) \in W$. U_h^{rs} denotes the reachability threshold, which defines the total number of recharging EVs capable of taking path $h \in P^{2,rs}$ because they have sufficient energy to reach the path's charging station link. Let $\zeta_h = \left[1 - F_T\left(\frac{E_{h,t}^{r\tilde{a}}}{E_{max}};\alpha^r,\beta^r\right)\right]$ denote the fraction of EVs with sufficient SOC to travel path $h \in P^{2,rs}$. Then, $\mathcal{E}_h$ is an index set that holds the indices i of all paths that require the same or more range than path $h \in P^{2,rs}$ for a given OD-pair $(r,s) \in W$; that is:

$$\mathcal{E}_h = \{i: \zeta_i \geq \zeta_h\}. \tag{15}$$

With this in mind, Eq. (13) states that the cumulative flow of recharging EVs on a path $h \in P^{2,rs}$ is less than or equal to the total number of vehicles able to reach its charging station, as travelers in range of a given charging station are a subset of those capable of traveling to charging stations that are even further away.

To visualize these constraints, consider the simple network shown in Fig. 4. It consists of seven nodes and nine primary links. There is one OD-pair (1-7) and four connecting paths. Let the paths containing charging stations be numbered from top to bottom $P^{2,1-7} = \{k_1, k_2, k_3\}$ and the path without a charging station $k_0 = P^{1,1-7}$. Path set $P^{1,1-7}$ is limited to a single path for illustrative purposes. In application, the vehicle class's full path set would include the paths with charging stations collocated by using the primary links.

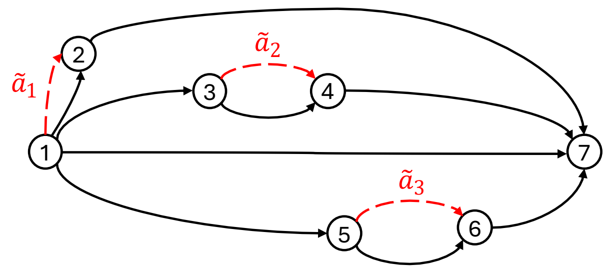

Figure 4 Example network for illustrating range constraint

Consider then, the distribution shown on the left in Fig. 5 and let it be the starting SOC distribution of the origin node 1. It is obvious that the charging stations are of different distances to the origin node. Therefore, different amounts of energy are required to reach each charging station. Given the continuous distribution of starting energy levels, there is only a certain fraction of the vehicle population, that is able to reach a given charging station.

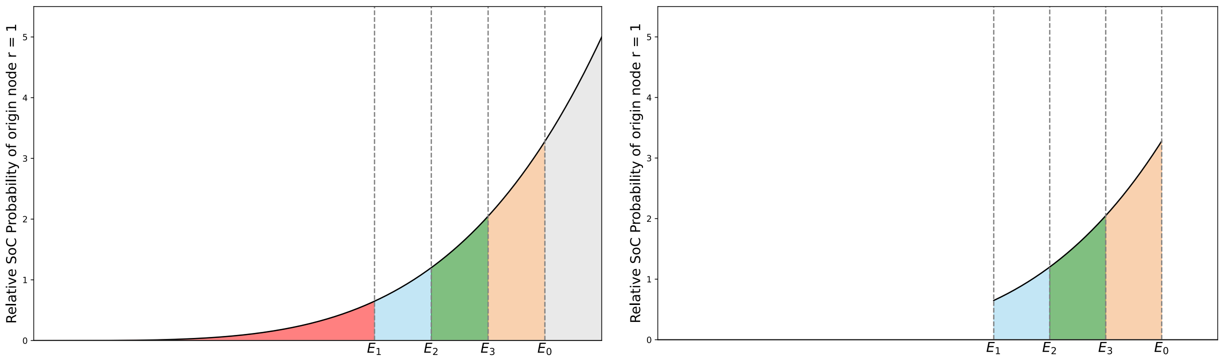

Figure 5 Division of recharging EVs $(m = 2)$ *into subsets based on starting SOC*

The vertical lines in the distribution show the starting energy required to reach each charging station, denoted by their respective path subscripts. It then becomes clear that the total area underneath the graph before any given energy level constitutes the fraction of vehicles unable to reach the charging station under consideration. Considering the above network, then, the red area before E_1 is the fraction of vehicles unable to reach the first (closest) charging station, which are therefore stranded at the origin node. This is the fraction of EVs calculated in Eq. (12b) with $F\left(\frac{E^{rs}_{\tilde{a},1}}{E_{max}};\ \alpha^r, \beta^r\right)$. Similarly, the last area past E_0 represents the fraction of EVs that are able to finish the shortest path $k_0 = P^{1,rs}$ between the OD-pair and are therefore counted towards $q^{1,rs}$. Clearly, then, only the area between E_1 and E_0 is relevant to the distribution of recharging vehicles ($m = 2$), which represents the total recharging vehicle demand. Hence, the starting SOC distribution is truncated between those boundaries and used for the definition of the range constraints in Eq. (14).

The resulting distribution is shown on the right side of Figure 5. For a given OD demand, the range constraints specify that the number of EVs visiting a particular charging station is, at a maximum, the total number of EVs able to reach it. This considers that an EV capable of reaching more than one charging station may visit any one of them. For instance, all vehicles with sufficient SOC to reach the furthest charging station $\tilde{a}_3$ also have sufficient range to reach the other two charging stations. Similarly, the sum of the areas between E_2 and E_0 characterizes all drivers able to reach $\tilde{a}_2$ and $\tilde{a}_1$. Hence, the constraint for this path dictates that this is the maximum number of EVs visiting $\tilde{a}_2$. Crucially, the drivers within range of $\tilde{a}_3$ are a subset of those in range of $\tilde{a}_2$. Therefore, the sum of their flows must satisfy Eq. (14), as stated in Eq. (13). Lastly, the closest charging station, $\tilde{a}_1$, is clearly the only one that only a certain fraction of drivers can reach. This is ensured through the range constraint in Eq. (13) (where $\mathcal{E}_h$ will only have one element) in conjunction with the flow conservation constraint in Eq. (3).

3.2.6. Problem Formulation

The behavioral model described in the previous section can be used to formulate the queueing-agnostic EV user equilibrium TAP with stochastic starting SOCs. It states that no EV travelers can unilaterally change between paths within their range to improve their cumulative travel and expected, VOT-adjusted charging time (generalized cost). The corresponding nonlinear optimization problem (NLP) can be constructed as:

$$\min_{f^1, f^2} Z = \sum_{a \in A} \int_0^{x_a(f)} c_a(\varsigma) d\varsigma + \eta \sum_{(r,s) \in W} \sum_{k \in P^{2,rs}} f_k^{2,rs} \frac{E_k^{rs}}{\bar{P}_{\tilde{a}}} \tag{16}$$

s.t.

$$\sum\nolimits_{k \in P^{m,rs}} f_k^{m,rs} = q^{m,rs}, \qquad \forall m \in M, (r,s) \in W \tag{3}$$

$$f_k^{rs} \geq 0, \qquad \forall k \in P^{rs}, m \in M, (r,s) \in W \tag{4}$$

$$U_h^{2,rs} - \sum_{i \in \mathcal{E}_h} f_i^{2,rs} \geq 0, \qquad \forall h \in P^{2,rs}, (r,s) \in W \tag{13}$$

Here, $f = [f^1, f^2]^T$ and $x_a(f)$ is defined through Eq. (5). Therefore $x_a(f)$ is affine in f since it represents the link flow as the sum of path flows using link $a \in A$. Note that Eqs. (3) and (4) are repeated from Section 3.2.1.

The first term of the objective function in Eq. (16) represents the Beckmann integral, which guarantees a user equilibrium (UE), as defined by Wardrop's first principle [44]. The second term is a path-specific constant and quantifies the cumulative perceived disutility incurred from charging, as defined in Eq. (11). The constraints (3) and (4) enforce flow conservation and non-negativity and the constraint (13) represents the range constraint and enforces the maximum flow on a set of paths below the range requirement for a given path $h \in P^{2,rs}$.

The Wardrop conditions for this two-class user equilibrium can be formulated as in [44], [50]:

$$f_k^{1,rs} > 0 \Rightarrow C_k^{1,rs}(x) = \mu^{1,rs}, \tag{17}$$

$$f_k^{1,rs} = 0 \Rightarrow C_k^{1,rs}(x) \geq \mu^{1,rs}, \tag{18}$$

$$f_k^{2,rs} > 0 \Rightarrow C_k^{2,rs}(x) = \mu^{2,rs}, \tag{19}$$

$$f_k^{2,rs} = 0 \Rightarrow C_k^{2,rs}(x) \geq \mu^{2,rs}, \tag{20}$$

where $C_k^{1,rs}$ and $C_k^{2,rs}$ describe the generalized path costs for the given vehicle classes, and $\mu^{1,rs}$ and $\mu^{2,rs}$ are the Lagrange multipliers representing minimal perceived travel cost between the OD-pair $(r,s) \in W$.

In other terms, Eqs. (17)-(20) state that any non-zero path flow for a given OD-pair must have minimal cost, meaning the OD-pair has optimal flow.

Optimality Conditions

To describe the optimality conditions and demonstrate the proposed NLP's optima reach a UE, equivalent to Wardrop's UE conditions, the Lagrangian, $\mathcal{L}(f^1, f^2, \mu, \lambda, v)$, is defined in Eq. (21) and from it the Karush-Kuhn-Tucker (KKT) conditions are derived.

$$\begin{aligned}\mathcal{L}(f^1, f^2, \mu, \lambda, v) = \sum_{a\in A} \int_0^{x_a(f)} c_a(\varsigma)d\varsigma + \eta \sum_{(r,s)\in W} \sum_{k\in P^{2,rs}} f_k^{2,rs} \frac{E_k^{rs}}{\bar{P}_{\tilde{a}}} \\ + \sum_{m\in M} \sum_{(r,s)\in W} \mu^{m,rs} \left(q^{m,rs} - \sum\nolimits_{k\in P^{m,rs}} f_k^{m,rs} \right) \\ + \sum_{(r,s)\in W} \sum_{h\in P^{2,rs}} \lambda_h^{rs} \left(\sum_{i\in \mathcal{E}_h} f_i^{2,rs} - U_h^{2,rs} \right) - \sum_{m\in M} \sum_{(r,s)\in W} \sum_{k\in P^{m,rs}} \nu_k^{m,rs} f_k^{m,rs}.\end{aligned} \tag{21}$$

Here, $\mu^{m,rs}$, λ_h^{rs}, and $\nu_k^{m,rs}$ are Lagrange multipliers corresponding to the constraints of the NLP.

The first order necessary conditions for the NLP are:

$$\frac{\partial \mathcal{L}(f^1, f^2, \mu, \lambda, v)}{\partial f^1} = \sum_{a\in A} c_a(x_a)\delta_{a,k}^{1,rs} - \mu^{1,rs} - \nu_k^{1,rs} = 0, \qquad \forall k \in P^{1,rs}, (r,s) \in W, \tag{22a}$$

$$\begin{aligned}\frac{\partial \mathcal{L}(f^1, f^2, \mu, \lambda, v)}{\partial f^2} = \sum_{a\in A} c_a(x_a)\delta_{a,k}^{2,rs} + \eta \frac{E_k^{rs}}{\bar{P}_{\tilde{a},k}} \\ + \sum_{h:k\in \mathcal{E}_h} \lambda_h^{rs} - \mu^{2,rs} - \nu_k^{2,rs} = 0, \qquad \forall k \in P^{2,rs}, (r,s) \in W.\end{aligned} \tag{22b}$$

These imply that for a given OD-pair, only paths with minimal perceived generalized cost carry nonzero flow.

For primal feasibility, the constraints (3), (4), and (13) must hold. For dual feasibility,

$$\lambda_h^{rs,*} \geq 0, \qquad \forall k \in P^{rs}, (r,s) \in W \tag{23a}$$

$$\nu_k^{m,rs} \geq 0, \qquad \forall k \in P^{rs}, (r,s) \in W, m \in M \tag{23b}$$

must be satisfied.

The complementary slackness terms are:

$$\lambda_h^{rs}\left(\sum_{i \in \mathcal{E}_h} f_i^{2,rs} - U_h^{2,rs}\right) = 0, \qquad \forall h \in P^{2,rs}, (r,s) \in W, \tag{24a}$$

$$\nu_k^{m,rs} f_k^{m,rs} = 0, \qquad \forall k \in P^{m,rs}, (r,s) \in W, m \in M. \tag{24b}$$

Convexity and Uniqueness

The BPR function for link flow delays,

$$c_a(x_a) = t_{0,a}\left(1 + \alpha_a \left(\frac{x_a}{Q_a}\right)^{\beta_a}\right), \tag{6}$$

is continuously differentiable, strictly increasing and convex. Therefore, the Beckmann integral, and, thus, the objective function in Eq. (16), are convex since the generalized charging cost added through Eq. (11) is a path-specific constant, which preserves convexity. The feasible region of the NLP is defined by affine constraints and therefore also convex. Thus, the NLP is a convex optimization problem, making any stationary point found using the KKT system a global minimizer.

Equivalence to Wardrop conditions

The first order necessary conditions Eqs. (22) represent the TAP's UE conditions. Notably, Eq. (22a) exactly matches the equilibrium conditions defined in Eqs. (17) and (18). To prove that the first order necessary condition for recharging vehicles matches Wardrop conditions, it must be recognized that the range constraint term $\sum_{h:k\in\mathcal{E}_h}\lambda_h^{rs}$ represents the constraints shadow price. This introduces additional costs for each path $h \in P^{2,rs}$ included in the set $\mathcal{E}_h$, thus accounting for all binding range constraints. Therefore, if active, the term's value is considered an increased cost that can be counted towards the total path cost. It follows from the convexity of the NLP and separability of its objective function that the first-order optimality conditions of the proposed optimization problem are equivalent to the UE conditions [50].

3.2.7. Solution Algorithm

This section provides a brief description of the solution algorithm used to solve the convex program formulated in the previous section. A detailed breakdown of the algorithm is presented in Appendix A1.

Traffic Assignment Problem

The proposed TAP is formulated as a path-based convex program with two vehicle classes. For fixed path sets, the optimization variables are path flows. Link flows are obtained from path flows using link-path incidence matrices (see Eq. (5)). Flow conservation is enforced through equality constraints (3). Nonnegativity of path flows and range constraints are enforced through the inequality constraints (4) and (13). The objective function is defined through Eq. (16) and consists of the Beckmann integral and path-specific generalized charging costs. The problem is implemented in MATLAB and solved using MATLAB's fmincon (interior-point) optimizer for constrained NLPs.

Column Generation

To avoid extraneous computation from path enumeration, the constrained NLP solver is nested in a column generation (CG) framework that computes the lowest cost paths for a given link flow solution and expands the path sets if the newly evaluated best paths are not yet included. The TAP solver execution is conducted with minimal, initial path sets $\{P_0^{1,rs}, P_0^{2,rs}\}, \forall(r,s) \in W$. $P_0^{1,rs}$ includes only the fastest paths without network loading. The initial path set for recharging EVs, $P_0^{2,rs}$, includes both the path with the lowest generalized cost, but also the feasible path with the shortest travel distance to any charging station. The latter must be included to ensure that range constraints can be satisfied. For later iterations, if the CG step adds at least one path to any set, the TAP solution procedure is repeated. Otherwise, it is considered to have converged with the given path sets, $\{P^{1,rs}, P^{2,rs}\}, \forall(r,s) \in W$.

To further minimize computational cost, the CG framework utilizes a phased approach. In the first phase, the solver utilizes relaxed parameters for the convergence threshold to enable faster convergence. This expedites populating the path sets. After converging using the first parameter set, the parameters are tightened and the algorithm continues running until convergence.

4. Charging Station Delay Modeling

The traffic assignment model presented in the previous section considers only expected charging power at a charging station location and is queueing-agnostic. It provides vehicle flows, $f_k^{2,rs}$, and their associated energy demands, E_k^{rs}, for each charging station link $\tilde{a} \in \tilde{A}$. But the aggregation of a variety of charging stations with differing charging powers (some low-power, some high power) into a single location in a link creates a set of charge points with heterogeneous output powers. This type of queue is difficult to represent using closed-form approximations due to the diverse set of output powers and path-dependent energy demands [51]. Therefore, a discrete-event Monte Carlo simulation is developed that models individual charging station locations as an M/G/c queue with a first-in first-out (FIFO) protocol and heterogeneous EVSE. This algorithm assigns EVSE to vehicles, and constrains their charging power according to the EVSE types and power limits.

4.1. Monte Carlo Simulation Framework

The Monte Carlo-based simulation framework receives as inputs the network data and the flows and associated energy demands of paths for each charging station location. These are aggregated into location-specific data structures. The structure of the framework is represented in Fig. 6, which can be divided into the following four computational steps (and one post-processing step not included in the figure):

1. Arrival Modeling
2. Energy Demand Assignment
3. Charging Station Assignment and Queue Management
4. EV Charging and Queueing Time computation

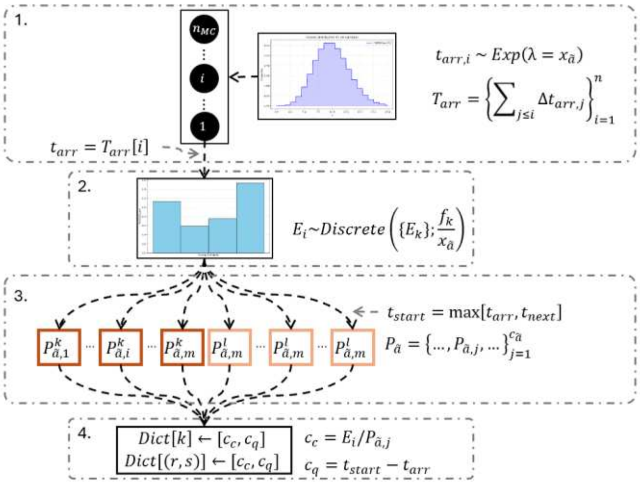

Figure 6 Monte Carlo simulation framework for charging station locations

Step 1: Arrival Modeling

The sample size of the Monte Carlo simulation is represented by n_{MC} discrete vehicles, which are assigned energy demands and EVSE. The commonly used Poisson process is used to model EV arrival times, t_{arr}, because of its memoryless property and empirical fit to random arrival patterns [52]. It represents a valid arrival model for disparate paths at a steady state, under the assumption that traffic dynamic effects such as platooning are negligible. This assumption is valid due to the small number of recharging vehicles relative to total traffic flows. To model arrival times, the Poisson process uses the cumulative sum of exponentially distributed inter-arrival times, $\Delta t_{arr,i}$ $[h]$, given by:

$$\Delta t_{arr,i} \sim Exp(\lambda = x_{\tilde{a}}), \tag{25}$$

where the arrival rate parameter, λ, is equal to the total flow rate of recharging vehicles, $x_{\tilde{a}} \left[\frac{veh}{h}\right]$,through the charging station location. This is, by construction, limited to recharging vehicles ($m = 2$). It can be calculated using Eq. (5), as:

$$x_{\tilde{a}} = \sum_{(r,s)\in W} \sum_{k\in P^{2,rs}} f_k^{2,rs} \delta_{\tilde{a},k}^{2,rs} .$$

Let the set of paths through link $\tilde{a} \in \tilde{A}$, then, be $K_{\tilde{a}} = \{k\colon \delta_{\tilde{a},k}^{2,rs} = 1,\ \forall (r,s) \in W\}$. Hence, the set of arrivals times, is given by:

$$T_{arr} = \left\{\sum\nolimits_{j\le i} \Delta t_{arr,j}\right\}_{i=1}^{n_{MC}} . \tag{26}$$

Arrivals are indexed chronologically and, therefore, processed sequentially.

Step 2: Energy Demand Assignment

The energy demand of vehicles visiting a charging station is path-specific. This means that each path $k \in K_{\tilde{a}}$ is associated with a distinct expected energy demand, E_k $[kWh]$. Therefore, a discrete sampling function is created that generates a random sample E_i for each arriving vehicle, based on the path-specific contribution of flow to the total EV flow, $x_{\tilde{a}}$, at a charging station location, given by:

$$E_i = Discrete\left(\{E_k\}, \frac{f_k}{x_{\tilde{a}}}\right). \tag{27}$$

Here, f_k represents vehicle flow on path $k \in K_{\tilde{a}}$. So, the sampling probabilities encode the likelihood that the energy demand of a randomly chosen EV corresponds to that of a given path.

Step 3: Charging Station Assignment and Queue Management

Randomly generated arrival times using a Poisson process represent the arrival times of individual EVs. Each charging station location $\tilde{a} \in \tilde{A}$ contains $c_{\tilde{a}}$ chargers with charging powers $P_{\tilde{a},j}$ $[kW]$ and timestamps by which they are available next, $\{t_{next,j}\}_{j=1}^{c_{\tilde{a}}}$. Let the set of all available EVSE upon the arrival of the EV i be:

$$\mathcal{A}_{\tilde{a},i} = \{j \in \{1, \dots, c_{\tilde{a}}\} : t_{next,j} \leq\ t_{arr,i}\}. \tag{28}$$

Then, an arriving EV i is assigned to the next EVSE, j_{next}, according to:

$$j_{next} = \begin{cases} \min[\mathcal{A}_{\tilde{a},i}], & if\, \mathcal{A}_{\tilde{a},i} \neq \emptyset \\ \min\left(\arg\min_j \left[\{t_{next,j}\}_{j=1}^{c_{\tilde{a}}}\right]\right), & if\, \mathcal{A}_{\tilde{a},i} = \emptyset \end{cases}. \tag{29}$$

If $\mathcal{A}_{\tilde{a},i} \neq \emptyset$, the EV is assigned to the available EVSE with the lowest index. The set of EVSE is ordered in descending power. Therefore, if there are more than one available EVSE, the assignment prioritizes higher power chargers. In cases where multiple equal power options are available, this also ensures a tiebreaker through the lowest index. Otherwise, $\mathcal{A}_{\tilde{a},i} = \emptyset$, the EV is assigned to the charger with the smallest next-available timestamp, with ties broken by the lowest index. The time by which the assigned charger is then available, t_{next}, is retrieved by indexing $\{t_{next,j}\}_{j=1}^{c_{\tilde{a}}}$ with j_{next}. The timestamps at which the charge event begins, $t_{star,i}$, is found with:

$$t_{start,i} = \max\left[t_{next}, t_{arr,i}\right]. \tag{30}$$

For each vehicle, the difference between their arrival time $t_{arr,i}$ and service start time $t_{start,i}$ corresponds to the queue delay $c_{q,i} = t_{start,i} - t_{arr,i}$ experienced by the i-th EV.

Once an EV is assigned to a charging station, its charging delay $c_{c,i}\ [h]$ is calculated deterministically through: [3]

$$c_{c,i} = \frac{E_i}{P_{\tilde{a},j_{next}}}, \tag{31}$$

where E_i is its previously sampled energy demand $[kWh]$ and $P_{\tilde{a},j}$ is the output power of the charging station $[kW]$ to which the i-th EV has been assigned. This marks the end of the customer's service, which serves as the time the charging station is available for the next customer, $t_{next,j_{next}} \leftarrow t_{start,i} + c_{c,i}$.

Step 4: EV Charging and Queueing Time Computation

The charging and queueing times experienced by travelers on different paths are aggregated by path, location and OD-pair. The framework consecutively simulates charging station locations. Therefore, the charging time is calculated using the stochastically generated energy demand and the deterministic power output of the charging station a customer is assigned to. The charging station energy demand is tied to a path, which in turn is tied to the OD-pair it is connecting. These relations enable the aggregation by both charging station and OD-pairs, enabling calculation of disaggregated resilience metrics (discussed in Section 5).

---

[3] The assumption of deterministic recharging times is defensible under constant power (CC-CV) charging profiles for vehicles at <80% SOC.

The queueing model is susceptible to unstable queues, which produce nonlinear queueing time growth. In queueing theory, queue-stability is characterized by the server utilization ρ [52]. The utilization of EVSE at the charging location $\tilde{a} \in \tilde{A}$ is calculated with:

$$\rho_{\tilde{a}} = \frac{\lambda \bar{E}_{\tilde{a}}}{\sum_{j \in c_{\tilde{a}}} P_{\tilde{a},j}} = \frac{x_{\tilde{a}} \bar{E}_{\tilde{a}}}{\sum_{j \in c_{\tilde{a}}} P_{\tilde{a},j}}, \tag{32}$$

where $x_{\tilde{a}}$ is the traffic flow through the charging station location link, $\sum_{j \in c_{\tilde{a}}} P_{\tilde{a},j}$ is the sum the output power of all EVSE at the location $\tilde{a} \in \tilde{A}$, and $\bar{E}_{\tilde{a}}$ is the mean path flow-weighted energy demand at the charging station location. The latter is calculated with:

$$\bar{E}_{\tilde{a}} = \frac{\sum_{k \in K_{\tilde{a}}} f_k E_k}{x_{\tilde{a}}}, \tag{33}$$

where it is reiterated that $K_{\tilde{a}}$ is the set of paths using the charging station link $\tilde{a} \in \tilde{A}$. This gives:

$$\rho_{\tilde{a}} = \frac{\sum_{k \in K_{\tilde{a}}} f_k E_k}{\sum_{j \in c_{\tilde{a}}} P_{\tilde{a},j}}.$$

Eq. (32), then, represents the utilization of the total output power capacity of a charging station location through the mean energy demand flow by incoming EVs $\left[\frac{kWh}{h}\right]$. Charging station locations are overutilized when $\rho_{\tilde{a}} > 1$, which results in unstable queues. Thus, steady-state queues at charging station locations only provide sensible queueing delays for:

$$\frac{\sum_{k \in K_{\tilde{a}}} f_k E_k}{\sum_{j \in c_{\tilde{a}}} P_{\tilde{a},j}} \leq 1.$$

This threshold is implemented as termination criterion for a charging station location's Monte Carlo simulation execution. When crossed, the resulting utilization is saved, and the queue is marked as unstable. Unstable queues result in queue delays growing indefinitely, making queueing and trip delays unbounded. Therefore, the trip and queueing time resilience values (see Section 5) of OD-pairs with unstable queues are excluded from considerations - instead being reported as unstable.

Step 5: Post-processing

To ensure repeatability, a fixed, large number of arrivals n_{MC} (=500,000) is chosen (see Appendix A3.2.1.), and a warmup set of the first w (=1,000) samples is removed from the recorded data. The latter additionally ensures that the resulting mean queueing and charging times are not skewed from the warmup of the simulation, since EVSE are instantiated empty.

5. Resilience Metrics

This section presents the resilience metrics that are derived from the performance measures produced by the modeling framework.

The function of a transportation system is to enable the movement of people, goods and services between two points. Therefore, the resilience metrics seek to quantify a system's capacity to satisfy existing travel demands when subjected to resilience events. The transportation system's functionality can be described using the dimensions of (i) overall accessibility – how much travel demand can be satisfied – and (ii) quality-of-service– how well the travel demands are satisfied. As a result, two metrics for the quantification of general resilience (Accessibility Resilience and EV Trip Time Resilience) that characterize these dimensions are proposed. Further, resilience measures to characterize each performance measure of the electrified transportation system are proposed (EV travel time resilience, charging time resilience and queueing time resilience). These resilience metrics are derived from the resilience index according to Eq. (2). Its integral is adapted to the equilibrium models as the sum of n discrete timesteps weighted by their respective durations T_i:

$$R = \frac{\int_{t_0}^{t_1} Q(t)\, dt}{t_1 - t_0} \Rightarrow RI = \frac{1}{t_1 - t_0} \sum_{i=1}^{n} T_i Q_i\,, \tag{34}$$

where Q_i is normalized performance (quality function) during the i-th timestep. Each timestep represents a discrete network state, which enables the modeling of recovery dynamics. Lastly, to provide insight into the level-of-service experienced by EVs compared to ICEVs, the relative travel time resilience is proposed.[4]

5.1. Accessibility Resilience

This thesis defines accessibility to electrified transport as the ability to satisfy travel demand given one's starting SOC, under the restrictions of the modeling framework (one charging stop per trip). The rate of stranded EVs is, therefore, quantified, by Eq (12b), as the number of EVs that is unable to travel to the closest charging station to their origin, that enables a feasible path to the destination on 80% SOC. To quantify accessibility of the electrified transportation system, first accessibility A^{rs} between an OD-pair $(r, s) \in W$ is defined as the fraction of EVs whose travel demand can be satisfied. Accessibility resilience, R_{str}^{rs}, is, then, defined as:

$$A^{rs} = \frac{1}{t_1 - t_0} \sum_{i=1}^{n} T_i \left[1 - \frac{q_{str,i}^{2,rs}}{\gamma^r q_i^{rs}}\right], \tag{35a}$$

$$R_{str}^{rs} = \gamma^r q_0^{rs} \frac{A^{rs}}{\gamma^r q_0^{rs} - q_{str,0}^{2,rs}}, \tag{35b}$$

where γ^r is the EV ownership rate of the OD-pair's origin zone, and T_i is the duration of the i-th timestep $[h]$. q_0^{rs} and $q_{str,0}^{2,rs}$, and q_i^{rs} and $q_{str,i}^{2,rs}$ are the total travel demand and number of stranded EVs per unit time at baseline and during timestep i, respectively.

---

[4] Temporal metrics (with units of time) for performance assessment are widely used in traffic analysis [53]. In the present research, their application is favored due to their ability to characterize the complex interdependencies between vehicles flows, network conditions, and exogenous parameters at an OD-pair-level in centralized measures.

Accessibility resilience, R_{str}^{rs}, represents the mean accessibility retention for EVs between an OD $(r, s) \in W$. Values near unity show strong retention of accessibility, whereas smaller values indicate the travel demands of an increased number of EVs cannot be satisfied during the disrupted system states.

5.2. EV Trip Time Resilience

EV Trip Time Resilience, R_{trip}^{rs} (Eq. 36a), describes the mean change in total trip time between a given OD-pair. It includes time spent on the road (travel time), waiting time in queue at a charging station (queueing time), and waiting time while recharging the vehicle (charging time). The superscripts '2' (which denotes the vehicle class m = 2 which requires recharging enroute) are omitted in the remaining discussions for clarity of notation.

$$R_{trip}^{rs} = \frac{1}{t_1 - t_0} \sum\nolimits_{i=1}^{n} T_i \left(\frac{c_{trip,0}^{rs}}{c_{trip,i}^{rs}} \right). \tag{36a}$$

c_{trip}^{rs} is the mean trip time EVs require to travel between a given OD-pair.

$$c_{trip}^{rs} = \frac{1}{q^{2,rs}} \sum_{k \in P^{2,rs}} f_k^{2,rs} \left(c_{tt,k}^{rs} + c_{c,k}^{rs} + c_{q,k}^{rs} \right) \tag{36b}$$

Eq. (36b) shows that this value is calculated as an average of the trip times of all paths connecting the OD-pair, weighted by their path flows f_k^{rs}. $c_{tt,k}^{rs}$, $c_{c,k}^{rs}$, and $c_{q,k}^{rs}$ are the generalized travel time, mean charging time, and mean queueing time on the k-th path, respectively. The path travel time is the sum of its link travel times (see Eq. 6). The mean trip time must be calculated because the respective delays may vary between paths. Variations between paths of the same OD-pair may arise from detours due to range restrictions and stochastic charging delays, requiring path-flow weighting to represent OD-specific means. In Eq. (36a), the trip time degradation is calculated. The normalization over the modeled period then yields the mean retained performance relative to the baseline (undisrupted) trip time, $c_{trip,0}^{rs}$. For example, a trip time resilience of 0.5 would mean that over the modeled duration, it takes EVs an average of twice as long to reach their destination.

5.3. Component Resilience Metrics

Since the total trip time of recharging EVs is comprised of travel, recharging, and queueing delays, it can be unclear which performance dimension is the primary contributor to an experienced level-of-service degradation. Therefore, a resilience metric for each performance dimension is proposed here to quantify the mean retained performance for each individual delay component relative to baseline. The performance dimension resilience can be calculated using:

$$R_D^{rs} = \frac{1}{t_1 - t_0} \sum_{i=1}^{n} T_i \left(\frac{c_{D,0}^{rs}}{c_{D,i}^{rs}} \right), \tag{37a}$$

$$c_D^{rs} = \frac{1}{q^{2,rs}} \sum_{k \in P^{2,rs}} f_k^{2,rs} c_{D,k}^{rs}, \tag{37b}$$

where $c_{D,0}^{rs}$ and $c_{D,i}^{rs}$ are the mean delays caused by dimension $D = \{tt, c, q\}$ at baseline and the i-th timestep, respectively. Similarly to the mean trip time, c_{trip}^{rs}, these delays must be calculated as the mean of the respective delays for all paths $k \in P^{2,rs}$ between an OD-pair $(r, s) \in W$. Hence, these are calculated in Eq. (37b) as path flow-weighted mean delays.

This template can then be applied to the individual performance dimensions to calculate travel time resilience, R_{tt}^{rs}, charging time resilience, R_c^{rs}, and queueing time resilience, R_q^{rs}. The individual performance measures for the latter two metrics, $c_{c,k}^{rs}$ and $c_{q,k}^{rs}$, are mean charging and queue times determined with the Monte Carlo-based simulation framework for the given path, $k \in P^{2,rs}$, at the charging station location the vehicle visits. The travel time experienced by EV operators for a given path, $k \in P^{2,rs}$, is calculated with Eq. (6), as the sum of its link travel times.

5.4. Relative EV travel time resilience

The constraints on the path choices for EVs that require recharging enroute might necessitate a large detour, which can cause a significant increase in time spent in transit. In contrast, because of the prevalence of gasoline stations and the associated capacity for quick refueling, it is assumed that conventional vehicle travel is functionally unconstrained by refueling. For EVs, the limited path set available with enroute charging might require the use of more congested road links. This leaves EV travelers vulnerable in hazard scenarios, in which detours might significantly amplify their travel times. To identify how these resilience aspects disproportionately affect EV travelers, the relative EV travel time resilience, $\hat{R}_{tt}^{rs}$, is proposed. It determines the relative increase in EV travel time compared to non-recharging vehicles and is calculated as:

$$\hat{R}_{tt}^{rs} = \frac{R_{tt}^{2,rs}}{R_{tt}^{1,rs}}, \tag{38}$$

where $R_{tt}^{1,rs}$ and $R_{tt}^{2,rs}$ are the travel time resilience values for non-recharging and charging vehicles as defined in Section 3. Hence, the relative EV travel time resilience quantifies the mean travel time performance loss experienced by EVs relative to vehicles not refueling enroute. For example, a value of $\hat{R}_{tt}^{rs} = 0.5$ indicates that the travel time of EVs, on average, is affected twice as much compared to ICEVs and EV that don’t recharge.

6. Case Study: Cameron Peak Wildfire

In this section a numerical example is provided to demonstrate the utility of the proposed methodology for resilience assessment. This case study is based on the 2020 Cameron Peak Wildfire in Northern Colorado, which persisted for several months, causing multiple evacuations and road closures throughout its duration [54]. Most importantly, it led to the closing of US-34, which represents the primary connecting link between the town of Estes Park and the Front Range region [55]. This disruption necessitated major detours for East-West travel in that region, whose knock-on effects on performance of the electrified transportation system can be quantified.

The case study seeks to develop this scenario as a model of wildfire and other resilience challenges to Northern Colorado's EV transportation networks, not to model historical occurrences or conditions. Modeling parameters and variables will be modified so as to stress-test the network model and thereby inform infrastructural and operational planning activities.

6.1. Data Sources and Model preparation

The spatial boundaries of the chosen system include the transportation network of Northern Colorado between the town of Fort Collins in the north, Greeley in the east, Estes Park in the West and the county border of Larimer County in the south. The network model was synthesized by extracting all major highways within the spatial boundaries of the analyzed area [56]. This preliminary network was overlayed with existing charging stations to allocate them to roadways based on proximity (see Section 3.2.1). Where charging stations could not feasibly be allocated to existing links, roads of lower functional classes were added to the network. The resulting network graph is shown in Fig. 7, where green roads indicate links with and black roads are links without charging stations allocated to them. In cases where charging stations are close enough to a node such that they cannot be reasonably assigned to a link, a "zero length dummy link" with no travel time is created that starts at a given node and feeds back into it. These links are represented in the figure by a green outline around a node. The red perimeter outlines the spatial expanse of the wildfire, and the dashed link connecting nodes 36 and 37 shows U.S. Highway 34, which closed to all traffic during wildfire scenario. Other rural roads affected by the wildfire were excluded from the analysis due their very small travel demands. The network consists of 63 nodes and 285 directed links. Each link's congestion behavior is characterized by its α_a and β_a parameters (see Eq. (6)). These are globally set to $\alpha_a = 0.15$ and $\beta_a = 4$, which aligns with common practice. Their free-flow travel time is calculated as a function of their length and the speed limit [57]. The travel capacity of road links was assigned based on their functional class and number of lanes according to publicly available data [56]. To that end, a generic per-lane capacity provided in [57] were assigned to functional classes as follows:

Table 1 Assigned per-lane road travel capacities, Q_a, based on functional class

Functional Class	**Per-Lane Capacity $\left[\frac{veh}{h}\right]$**
1	2400
2	1400
3	1000
4	800
5	800

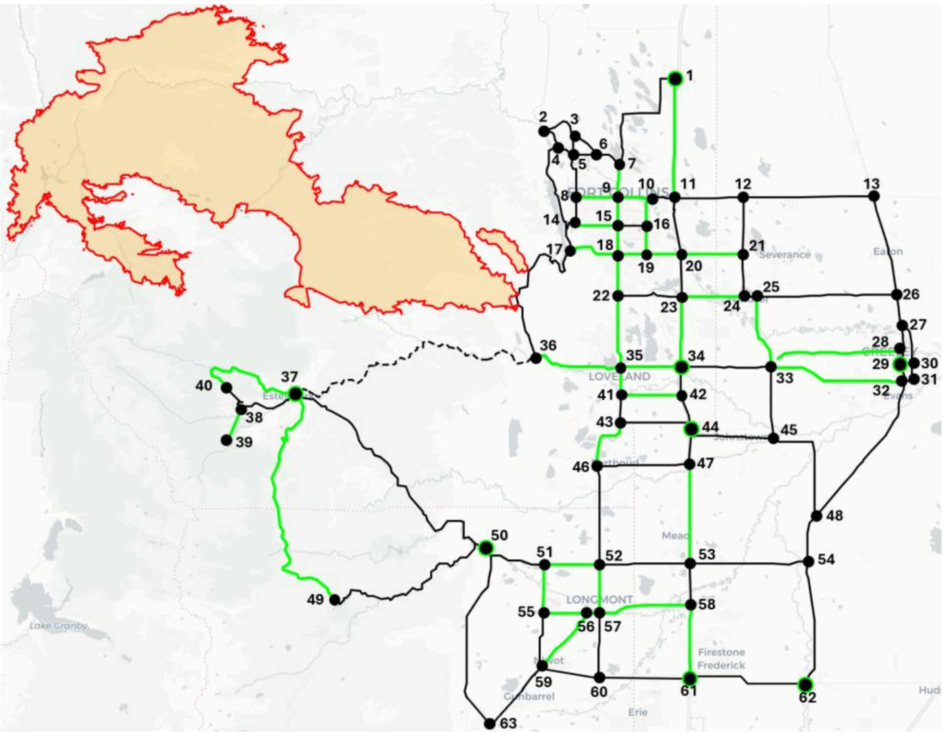

Figure 7 Northern Colorado Region with traffic network and the area affected by the Cameron Peak wildfire

The expected output power $P_{\tilde{a}}$ assigned to charging station links is determined using:

$$P_{\tilde{a}} = \begin{cases} P(n_{L2}, n_{L3}), & n_{L3} < 15 \\ P_{L3}, & n_{L3} \geq 15 \end{cases}, \tag{39}$$

with:

$$P(n_{L2}, n_{L3}) = \frac{n_{L2} P_{L2} \left(1 - \frac{a}{n_{L2} + a}\right) + b n_{L3} P_{L3} \left(1 - \frac{a}{b n_{L3} + a}\right)}{n_{L2} + b n_{L3}}, \tag{40}$$

where n_{L2} and n_{L3} are the number of level 2 (L2) and level 3 (L3) charging stations on a given charging station link $\tilde{a} \in \tilde{A}$, P_{L2} and P_{L3} are the constant output powers of L2 and L3 chargers, and a and b are scale parameters. a determines the weighting of both stations station levels, thereby influencing the slope at which the expected output power increases with the number of stations at a link. b only applies to L3 charging stations and defines how much more their presence contributes to the overall expected output power. This models an $\frac{b}{a}$-fold preference for L3 over L2 charging stations. Fig. 8 shows the surface plot of $P_{\tilde{a}}$ for the parameters used in the case study: $a = 1$, $b = 3$, $P_{L2} = 14kW$, and $P_{L3} = 50kW$ [58].

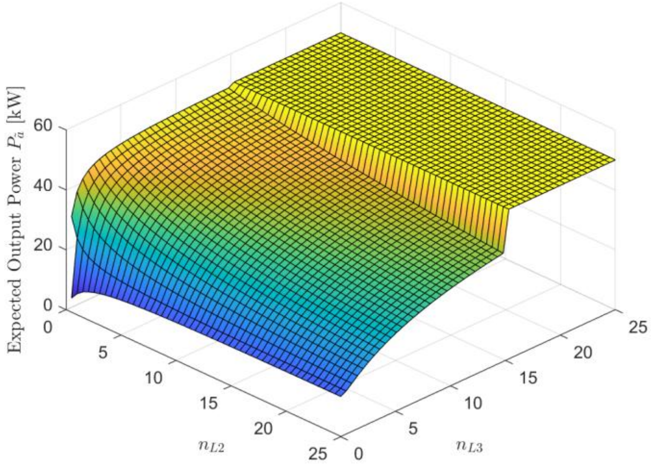

Figure 8 Estimation of expected charging power as a function of the number of charging stations of different power levels

No high-granularity data on EV ownership within Larimer County is publicly available. Therefore, every origin node is assigned to the county-level EV ownership rate of $\gamma = 0.0452$ (4.52%) [59]. The value-of-time (VOT) of charging and queueing, relative to driving is chosen was to be $\eta = 2.0$ [60], representing that EV users are willing to trade-off 1h of waiting for 2h of driving. The choice of η is subject to a high degree of uncertainty given the large degree of intra-population variability and large number of influencing factors [60]. However, a sensitivity study has been conducted to show that resilience results are consistent across the parameter's feasible range (Appendix A.3.3.2). As stated in Section 3.2.3, starting energy is modeled using a Beta distribution with parameters of $\alpha = 1.5$ and $\beta = 1.0$. The EV characteristics for the case study were an effective battery capacity (0-80% SOC) of $E_{max} = 75kWh$ and an energy consumption of $u = 0.35\frac{kWh}{mi}$, or $0.2175\frac{kWh}{km}$.

Travel demands for the modeled area were available from the Colorado Department of Transportation (CDOT). The data provided consisted of average annual daily travel (AADT) demands based on a source network of 1,151 centroids. To map the demands onto the analyzed network, shown in Fig. 7, each network's nodes are assigned coordinates. Based on these, the source network's nodes are assigned to nodes of the analysis network based on proximity with a cut-off radius of 5 km to avoid overallocation of demand from rural areas. Finally, the resulting trip data is limited to trips with a demand > 0.1 AADT. For this case study, peak hour traffic demand is adopted, to test a high-strain scenario. The AADT trips are transformed into peak-hour demand by multiplying the final OD-demand matrix by 0.093 [57]. This results in an OD matrix with 3,297 OD-pairs for the depicted network.[5] The total travel demand OD matrix $\boldsymbol{Q}$ is

---

[5] Despite being connected to I-25, which might introduce significant through and trans-boundary traffic, only internal traffic demands are considered for this case study.

disaggregated into the vehicle-class-specific OD matrices, $\boldsymbol{Q^1}$ and $\boldsymbol{Q^2}$. To reduce ill-conditioning caused by numerous very small-demand OD-pairs, the lowest demand OD-pairs are pruned from each class-specific OD matrix until the cumulative removed travel demand equals 5% of the respective matrix's travel demand totals. To preserve consistency for the relative EV travel time resilience $\hat{R}_{tt}^{rs}$, all OD-pairs present in $\boldsymbol{Q^2}$ are retained in $\boldsymbol{Q^1}$, even if they would otherwise have been pruned.

6.2. Scenario Definitions

The 2020 Cameron Peak wildfire began on August 16th and was declared fully contained by December 2nd. It was the biggest wildfire in the history of Colorado and caused significant damage. Over its course, several areas were evacuated, and two major highways and numerous local roads were closed [54]. For this numerical study, most affected roads are excluded from the network. The only affected road included in the network, highway US-34, is shown as a dashed line in Fig. 7. It was closed for a span of roughly 72 hours, between October 16th [54] and October 19th [61].

This case study considers two variants of the described wildfire scenario. The first scenario mirrors the impacts of the 2020 Cameron Peak wildfire, with the disruption being modeled as the removals of links between nodes 36 and 37, representing the closure of US-34. A second scenario of the case study expands this disruption by including the common-mode failure of the power grid supporting the charging station location at node 37. Along with this power outage, a reduced starting SOC of EVs departing from node 37 is modeled with $\alpha^{37} = \beta^{37} = 1.0$.

Due to the two-state comparison (no closure vs. closure), the disrupted period is represented as a single disrupted state ($n = 1$). Under the steady-state assumption, the weighting of performance metrics by the state's duration, T_i, therefore, does not change the computed resilience values. To enable comparability between the baseline and disrupted state, any hypothetical evacuations of Estes Park and other zones are excluded from the operational boundary of the analysis.

6.3. Results Scenario 1

Using the methods presented in this thesis, the system's behavior can be simulated by first solving the proposed traffic assignment model. The TAP solution provides (i) the number of stranded EVs, (ii) travel times between the different OD-pairs, and (iii) path flows through the various charging station locations with associated energy demands. These results are used to parameterize the Monte Carlo simulation, which yields mean charging and queueing times at each charging station location and for all paths and OD-pairs. Based on these measures, the proposed resilience metrics can be computed and compared. Here, accessibility and trip resilience serve as the primary basis for resilience evaluation of the network. Then, the performance component metrics are utilized as a diagnostic tool for identifying drivers of performance degradation.

Although the proposed resilience metrics can be computed for a sequence of discrete network states, this case study only has a single disrupted state. This is consistent with traffic network states during the wildfire, where the road was closed for 3 days and then reopened, without notable recovery or repairs. Therefore, its resilience metrics present a special case, where $n = 1$ and $T_1 = t_1 - t_0$, reducing each of the proposed resilience metrics (Section 5) to a state-wise comparison (baseline vs. disrupted) that yields relative performance retention rather than recovery dynamics. It is assumed that remaining recovery dynamics, such as traffic transients, can be neglected as their duration is short relative to the disrupted period.

Under the default resilience scenario, we find that the electrified transportation network performed well under disrupted conditions. The trip resilience values of all nonnegligible OD-pairs exhibit a median of 1.000, with the 10th percentile at 0.986. Only 12 OD-pairs experienced increased total trip delays of >11% ($R_{trip}^{rs} < 0.90$), which make up approximately 0.52% of the total travel volume of recharging EVs. This suggests that OD-pairs and EV travelers were largely unaffected and the effects of the disruption concentrate on a small, localized subset of OD-pairs. No increase in stranded EVs between the baseline and disrupted network states was found. Recharging EVs performed only marginally worse than NRVs across the metrics considered.

6.3.1. Traffic Assignment Results

The equilibrium flows computed in the TAP show that the network disruption yields a traffic flow redistribution of the vehicle flows utilizing the disrupted link. At baseline the two directed links connecting nodes 36 and 37 carry $152.3\frac{veh}{h}$ and $149.9\frac{veh}{h}$, respectively. These are removed under the disruption, causing these vehicle flows to be redirected along a detour, extending the travel distance of several OD-pairs. These redistribution patterns are displayed in Fig. 9, which shows the case study's network graph with its links colored according to the change in vehicle flow they exhibit between network states. Red links indicate an increase in vehicle flow, whereas blue links indicate a reduction in vehicle flows.

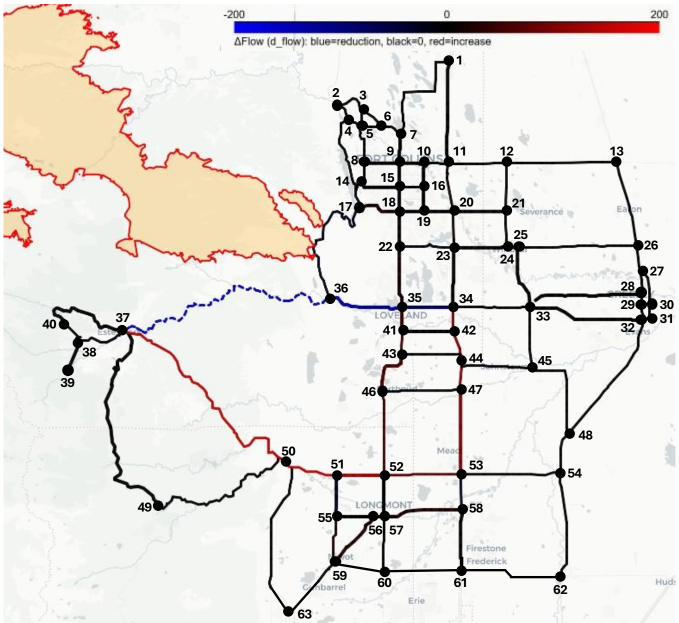

Figure 9 Vehicle Flow Redistribution between network states (baseline vs. disrupted)

The flow changes shown in Fig. 9 are consistent with the diverted flow around the closure of link 36-37, as the sum of redirected traffic through the north-south corridors of the network closely match the flow through the disrupted link to within $< 2\frac{veh}{h}$.

The equilibrium flows produced by the TAP yield path flows for recharging EVs, which each must visit a charging station link enroute. Aggregating these path flows and their associated energy demands yields charging station utilizations. These utilizations change slightly with the redistribution of traffic, as the feasibility and generalized costs of paths change. Fig. 10 shows the changes in utilization at charging station locations, $\Delta\rho$, between network states for all locations with $|\Delta\rho| > 10^{-5}$. These redistribution patterns are consistent across a range of feasible EV penetration parameters (see Appendix A.3.3.1).

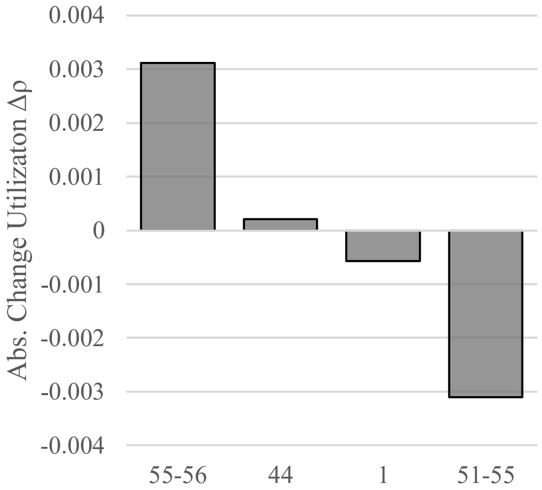

Figure 10 Charging Station Utilization change between network states in Scenario 1

The largest change in utilization was experienced by the charging station links 55-56 and 51-55. Other links experienced significantly smaller changes and were largely negligible.

The small values of $|\Delta\rho|$ (<1%) indicate that the disruption to the network did not sufficiently affect the expected trip delays of travelers to justify a change of charging station location choice.

The most highly utilized charging station location shows $\rho_{44} = 0.352$ (35.2%), thereby remaining far below saturation. In both network states the charging station utilization is concentrated at higher capacity charging station locations, where the charging station links with the top 5 largest charging demands service 57.7% (baseline) and 57.8% (disrupted) of the total charging demand of recharging EVs. The negligible increase in utilization concentration at the top-5 highest utilization links further indicates that the disruption does not materially relocate EV flow towards a smaller set of charging station links.

From the charging demands, charging and queueing delay estimates are derived using the Monte Carlo simulation framework. For a given network state, each charging station location was simulated with 1,000,000 Monte Carlo iterations and a warm-up set size of 1,000. These parameters produce stable convergence of delay metrics at an OD-pair-level at the given utilization-levels (see Appendix A.3.2.1).

6.3.2. Accessibility Resilience

In each network state, the total number of stranded EVs is $2.31\frac{veh}{h}$. Therefore, accessibility does not change and $R_{str}^{rs} = 1$ for every OD-pair $(r, s) \in W$. The accessibility of EVs to electrified transportation is based on network topology and the starting energy distribution of origin nodes. In the analyzed scenario, starting SOC distributions are not altered and the closure of a single road is simulated, which does not affect the distance to the closest charging station for the origin of any OD-pair.

6.3.3. Trip Time Resilience Results

Under this default resilience scenario, the electrified transportation network did not exhibit a drastic loss in functionality. The majority of OD-pairs showed only minor increases in delays for recharging EVs, while the most severe effects are concentrated on a small subset of OD-pairs. This finding is illustrated in Fig. 11, which shows the counts of OD-pairs by their trip time resilience, binned in intervals of 0.01 or 1%. It consists of 1640 OD-pairs with nonnegligible travel demand as determined by the exclusion rule from Section 6.1. The resilience performance of the network under stress is visible in the small number of OD-pairs with $R_{trip}^{rs} < 0.98$ (106 out of 1640, or 6.5%), which accounts for 5.1% of the total recharging EV travel demand $\left(28.1\frac{veh}{h}\right)$. Only 12 ($\approx$ 0.7%) exhibit $R_{trip}^{rs} < 0.9$, indicating that the disruption impacts are locally concentrated on the small left tail (see Fig. 11) of OD-pairs.

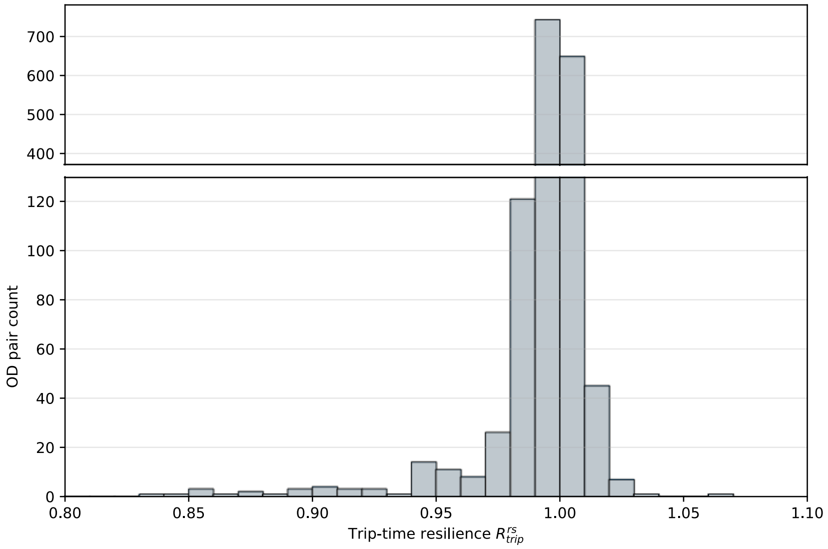

Figure 11 OD-pair Trip Resilience Counts binned by 0.01

6.3.4. Performance Resilience Results

The OD-pairs with reduced trip resilience values are disproportionately affected by (i) travel delays, and (ii) charging delays. To further investigate the performance degradation of the network, selected OD-pairs with a trip resilience $R^{rs}_{trip} < 1.0$ are highlighted, to illustrate distinct performance-loss mechanisms. This subset enables the demonstration of the diagnostic capabilities of the proposed resilience metrics. The OD-pairs are shown in Table 2 in ascending order of the trip-time resilience values R^{rs}_{trip} alongside their component resilience values for travel time (R^{rs}_{tt}), charging delay (R^{rs}_{c}), and queueing delay (R^{rs}_{q}), the relative EV travel time resilience ($\hat{R}^{rs}_{tt}$) and corresponding travel demands $q^{2,rs}$.

Table 2 Resilience metrics for illustrative set of OD-pairs with different performance-loss mechanisms

Nr.	Origin-Destination Pair	R^{rs}_{trip}	R^{rs}_{tt}	R^{rs}_{c}	R^{rs}_{q}	$\hat{R}^{rs}_{tt}$	$q^{2,rs}\left[\frac{veh}{h}\right]$
1	37-17	0.834	0.764	1.00	1.00	1.00	0.00573
2	4-37	0.958	0.951	0.972	2.93	1.16	0.00492
3	52-35	0.980	0.961	0.997	0.779	0.964	0.0442

The trip time resilience values range from 0.834 to 0.980, showing moderate performance degradations. Each OD-pair in Table 2 contains node 37 as origin or destination. This reflects a trend seen in the network's overall resilience, where most of the heavily-affected OD-pairs seen in the left tail in Fig. 11 have the origin or destination in the node cluster that was cut off by the road closure (nodes 37, 38, 39, 40). Consequently, their trip resilience values are dominated by travel delay increases. These delays equally affect recharging and non-recharging vehicles $\left(\hat{R}_{tt}^{rs} \approx 1\right)$. An example of such an OD-pair can be seen in Table 2, line 1, which shows that recharging EVs traveling between nodes 37 and 17 experience ~20% trip delay increase $\left(R_{trip}^{37-17} = 0.834\right)$. In this case, the performance resilience metrics show that only the travel delay is noticeably increased, suggesting that the travel delay increase is caused by the detour required to circumvent the road closure. Crucially, charging and queueing delays related to EV charging do not show changes, which indicates that the present charging infrastructure is adequate for accommodating the rerouting of vehicles. This pattern is represents the 46 OD-pairs (2.8%) with the lowest R_{trip}^{rs}-values, suggesting that the network's resilience performance is not bottlenecked by the charging infrastructure.

Other OD-pairs exhibit $\hat{R}_{tt}^{rs} < 1.00$, which shows that travel delays increase more for recharging EVs than NRVs over the disrupted period. Such is the case for OD-pair 52-32 $\left(\hat{R}_{tt}^{52-35} = 0.964\right)$. This suggests that the disruption requires a subset of recharging EVs travelling between the OD-pair to take a longer detour (compared to NRVs) during the disrupted network state(s) to visit charging station links. In this case, the path flows of the OD-pair 52-32 are predominantly assigned to charging station link 52-51. The increased congestion at this link in the disrupted state (Fig. 9) increases delays incurred when traversing it. Unlike NRVs, recharging EVs travel between the OD-pair 52-32 must travel on that link twice, to reach their destination, consequently incuring this increased travel delay twice, increasing their overall travel delays more than NRVs (as reflected in $\hat{R}_{tt}^{52-35} = 0.964$).

OD-pairs exhibiting $\hat{R}_{tt}^{rs} > 1.00$, show that travel delays increase more for NRVs than recharging EVs. Exemplary of this is the OD-pair 4-37 whose path flows are redistributed from largely visiting the charging station link at node 1 at baseline, to paths incorporating link 52-51 during the disrupted state. The avoidance of this detour in the disrupted network state yields reduced travel delays. In turn travelers visit the charging station link that is significantly further from their starting location, increasing charging delays and trip delays overall, as reflected in $R_{trip}^{4-37} = 0.958$.

This rerouting of recharging EVs coincides with different charging station link choices and different charging demands. These changes may drive increased charging delays, as EVs may recharge at lower-power EVSE or require more energy compared to the baseline network state. Such is the case for OD-pair 4-37 (Table 2, lines 2), as indicated by $R_{c}^{4-37} = 0.972$. At baseline, the lowest cost path incorporates the charging station link at node 1, with an energy demand of 36.02kWh. During the disrupted network state, 75.8% of that flow is redirected to a path incorporating the higher-capacity charging station link at node 44, where EVs recharge 39.35kWh because the charging station link is further from the OD-pair's origin. Both links only have L3 EVSE ($n_{L3,1} = 4, n_{L3,44} = 12$) assigned to them. Therefore, the effective charging power for each charging event is equal ($P_{L3} = 50kW$). This indicates that the observed increase in mean charging delays is driven by the increase in energy demand per charge event. Conversely, the lower EVSE count at node 1 makes it more susceptible to transient queues, whereas the charging station link at node 44 has higher capacity. Therefore, queueing delays improve in the disrupted state, as indicated by $R_{q}^{4-37} = 2.93$.

Due to the low utilization at charging station locations. Queueing delays are small relative to overall trip delays. This drives large volatility in queueing resilience values, as queueing delays are the only performance component, which can feasibly range from 0 to ∞. To visualize the contribution of individual performance dimensions to the trip delays, consider Fig. 12. It shows the changes of trip delays experienced by the OD-pairs highlighted in Table 2 in a stacked column diagram, where each segment shows the relative contribution of each performance component to the trip delay. For each OD-pair the right column represents the baseline trip performance and the left column represents the disrupted trip performance. Both columns are normalized by the trip delay at baseline, such that the right baseline-column serves as reference of the delay increases.

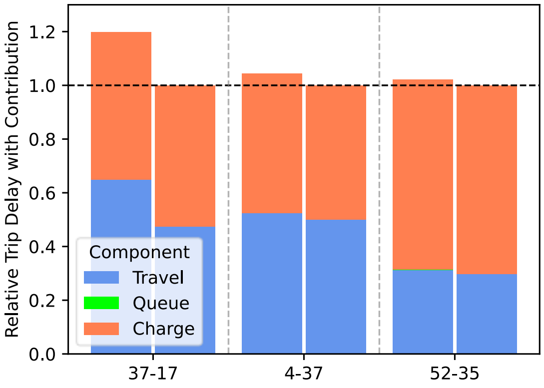

Figure 12 Performance Metric-level decomposition of trip resilience values for OD-pairs from Table 2

The figure shows that queueing delays are visually undetectable in the columns, making them largely negligible w.r.t. trip delays. These small values make the ratio-based resilience metric R_q^{rs} sensitive to fluctuations, which explains the large deviation in queueing resilience values in lines 2 and 3 of Table 2, that is, however, not reflected in the respective overall trip resilience values.

6.4. Results Scenario 2

This section shows the model and resilience results of scenario 2, in which the loss of charging power at node 37 is added to the disruption of the links between nodes 36 and 37. The results are compared to the results of scenario 1 from the previous section and show that charging station location at node 37 plays a pivotal role in ensuring the resilience of OD-pairs departing from the region west of link 36-37, when subjected to the closure of Highway US-34. Compared to the first scenario, the number of stranded EVs increases by 8.6%, and the number of OD-pairs with $R_{trip}^{rs} < 0.9$ increases from 12 to 72, with the $\min\left(R_{trip}^{rs}\right)$-values of the most heavily affected OD-pairs significantly degrading from 0.835 to 0.238.

This result is driven by the redistribution of charging demand, originating in the cut-off node cluster, to charging station links, that cannot provide the same level of charging power and capacity as the location at node 37, thereby degrading trip delays.

6.4.1. Traffic Assignment Results

The charging station location at node 37 serves as central provider of charging for EVs originating in the region that is cut-off by the disruption of link 36-37. At baseline it serves 76% of all recharging EVs departing from nodes 37-40 ($0.814\frac{veh}{h}$ out of $1.07\frac{veh}{h}$). The removal of the node introduces are large shift in the utilization of charging station locations of the network. This shift is further increased by the change of α^{37}, which reduces the mean starting SOC of EVs departing from 37, increasing the total volume of recharging EVs departing from node 37 from $0.575\frac{veh}{h}$ to $1.29\frac{veh}{h}$. Fig. 13 illustrates the absolute change in charging station utilization, $\Delta\rho$, between the equilibrium flows at baseline and the disrupted network state of scenario 2 for all charging station links with $|\Delta\rho| > 10^{-2}$, illustrating the redistribution of charging demand resulting from the disruption modeled in scenario 2.

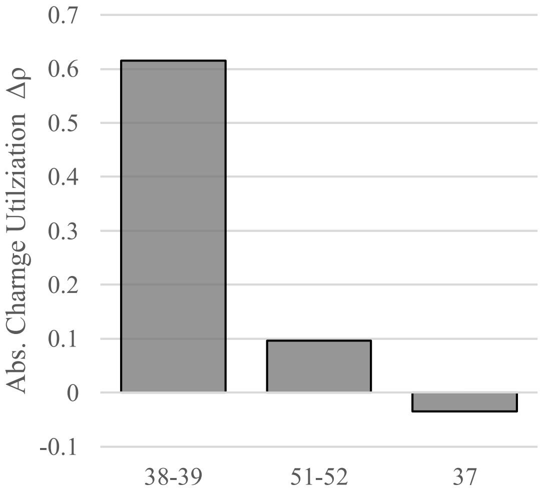

Figure 13 Charging Station Utilization change between network states in Scenario 2

The figure shows that the link at node 37 loses its entire utilization ($\Delta\rho_{37} = -0.035$). This charging demand is largely redistributed to surrounding charging station links. The redistribution of charging demand, as well as the overall increased number of recharging EVs departing from node 37 explains the large increase in utilization at links 38-39 and 51-52. Due to the reduced number of EVSE at these locations, their utilization increases disproportionately to that of the location at node 37.

6.4.2. Accessibility Resilience

The charging station link at node 37 represents the closest charging station for EVs departing from node 37. Removing it requires recharging EVs departing from node 37 to visit a different, further charging station, increasing the number of stranded EVs. Because the removed charging station link is directly at node 37, in scenario 1, there are no stranded EVs for any OD-pair departing from node 37. Conversely, in the disrupted network state of scenario 2, the total number of stranded EVs for all OD-pairs with node 37 is $0.203\frac{veh}{h}$. This increases the total number of stranded EVs from $2.31\frac{veh}{h}$ to $2.51\frac{veh}{h}$. The accessibility resilience values are zero, as the baseline network state exhibits no stranded EVs for all these OD-pairs.

6.4.3. Trip Time Resilience Results

Compared to the results of scenario 1, scenario 2 exhibits a significant degradation of functionality. While the impact of the disruption is also focused on a small subset of OD-pairs, its magnitude is significantly larger. This finding is illustrated in Fig. 14, which shows the counts of OD-pairs by their trip time resilience, binned in intervals of 0.01 or 1%. It consists of 1631 OD-pairs (compared to 1640 in scenario 1)[6].

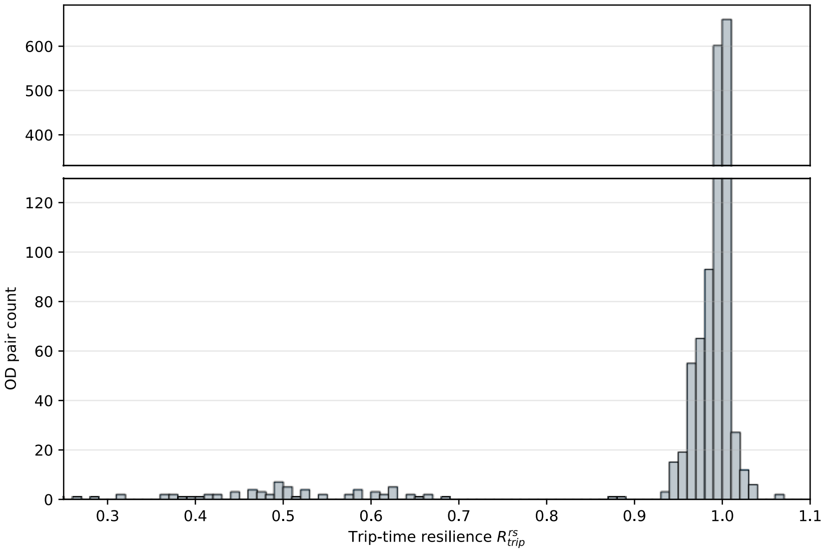

Figure 14 Charging Station Utilization change between network states (baseline vs. disrupted) of the modified disruption scenario (road closure + node 37 charging removed)

The figure shows a significant degradation of the network's resilience performance as illustrated by the greatly reduced R^{rs}_{trip}-values within the left tail of the distribution. Table 3 shows a set of

---

[6] This decrease is caused by the filtering of OD-pairs discussed in Section 6.1. The change in α^{37} increases the travel demand of recharging EVs departing from node 37, pushing 9 OD-pairs underneath the filter threshold.

summary statistics characterizing the degradation of the resilience performance with the loss of the charging station location in node 37. It includes the arithmetic mean and median of R_{trip}^{rs}-values over $(r, s) \in W$, the lowest R_{trip}^{rs}-value, the number of OD-pairs with $R_{trip}^{rs} \leq 0.9$, and the total number of excess stranded EVs compared to the baseline.

Table 3 Summary Statistics comparing the resilience performance of the networks in scenario 1 and scenario 2

Statistic	**Scenario 1**	**Scenario 2**
Mean R_{trip}	0.996	0.975
Median R_{trip}	1.00	1.00
$\min\limits_{(r,s)\in W}\left(R_{trip}^{rs}\right)$	0.835	0.238
$N\left(R_{trip} \leq 0.9\right)$	12	72
$\Delta\left[\sum\limits_{(r,s)\in W} q_{str}^{rs}\right]$	$0.0\,\frac{veh}{h}$	$0.203\,\frac{veh}{h}$

The table results support the qualitative findings from Fig. 14. The mean of the trip resilience values drops under the influence of the more heavily affected tail, while the median remains largely unchanged, showing that the loss of the charging stations at node 37 has a highly localized effect. This effect, nevertheless, dramatically degrades the trip time resilience of a subset of OD-pairs as indicated by the reduction in the lowest R_{trip}^{rs}-value.

6.4.4. Performance Resilience Results

The loss of EVSE at node 37 increases the distance that recharging EVs departing from that node must travel to reach the next closest charging station location, which requires a 5.8km detour. This increases the required starting energy for EVs to be able to depart on their trips by 1.26kWh[7],

---

[7] Based on the consumption constant of 0.2175 $\frac{kWh}{km}$ defined in Section 6.1

which increases the number of stranded EVs by 0.0203 $\frac{veh}{h}$, or 3.0% of the total travel demand of recharging EVs.

The degradation of the highly-affected OD-pairs is driven by charging and queueing delays as illustrated in Fig. 15, which shows the component-wise breakdown of the trip time resilience results for three of the bottom-7 OD-pairs. The displayed OD-pairs have been selected based on the difference in location of their destination within the network model.

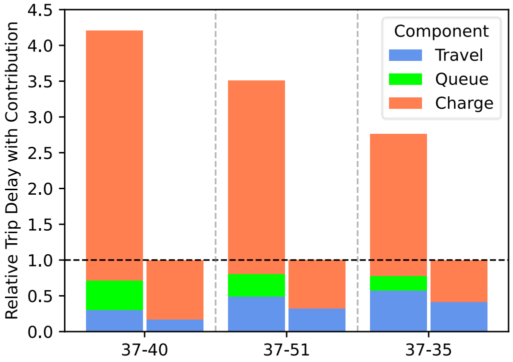

Figure 15 Performance metric-level decomposition of trip resilience values for three of the seven most affected OD-pairs in scenario 2

The figure shows that the primary driver behind the trip resilience degradation of OD-pairs is the large increase in charging delays. This increase is consistent with a lack of L3 EVSE at alternate charging station locations. Additionally, significant queueing delays are introduced, further degrading the trip resilience, which is consistent with the shift in charging station link utilizations (Fig. 13) alongside the reduced charging capacity of alternate locations.

7. Discussion

The resilience of the Northern Colorado network was evaluated when subjected to road closure conditions present during the 2020 Cameron Peak wildfire as well as the additional power outage at node 37. The results show that the electrified road transport, on the whole, has a high resilience to the road closure of US-34, between nodes 36 and 37, with only a small set of OD-pairs experiencing moderate delay increases and no measurable loss of accessibility (stranded EVs). The loss of electricity at node 37 severely increases the degradation of resilience while remaining localized to a subset of OD-pairs. The concentration of performance degradation is a central finding, as it demonstrates localized vulnerabilities of the electrified transportation system to the modeled disruption.

To understand the implications and capabilities of the modeling framework proposed here, this discussion section investigates the disaggregated contributors to resilience, plausible additional mechanisms that may affect performance dimensions, and the framework's application to assessment of interventions.

7.1. Holistic Performance View on Resilience of the Electrified Transportation System

Previous authors have evaluated the resilience of electrified transportation systems through the lens of charging station utilization [35], [36], [37] and satisfaction metrics [33], [34]. These approaches, while yielding valuable insights into the extent to which charging stations serve their purpose, do not capture network-level effects such as increases in travel time due to detours or charging-related delays from changes in route-choice behavior or increased congestion.

This proposed methodology, on the other hand, provides aggregate metrics that capture holistic temporal performance dimensions of both conventional and electrified transport using accessibility and trip delays as high-level performance metrics. The latter can be disaggregated into its performance dimensions, travel, charging and queueing delays, enabling the identification of network effects brought on by changes in travel behavior.

The above case study above shows that OD-pairs can be divided into two categories: 1) directly affected OD-pairs, whose connecting paths from the baseline scenario were rendered infeasible due to the disruption, and 2) indirectly affected pairs, that were affected by the rerouted traffic. The latter demonstrates that the framework is adequate for characterizing network effects induced by disruptions. An illustrative set of OD-pairs was discussed that demonstrates that the interpretability of the chosen resilience metrics with respect to one another. It should be noted that due to the travel demand threshold (Section 6.1), several nodes representing smaller zones are not included in the OD-pair set W, while other larger zones are overrepresented (e.g. Longmont, Fort Collins). The omission of negligible EV flows is justified because (i) queueing and charging delays are derived from stochastic arrivals, which introduce uncertainty for small flows, (ii) OD-pair-level traffic demand assignment to paths can cause disproportionate relative changes in computed ratios, and (iii) small flows have reduced network-level impact.

7.2. Disaggregation of Resilience by Performance Dimensions, and Delay Mechanisms

Viewing resilience of electrified travel through the lens of total trip delay (decomposable into the sum of travel, charging and queueing delays) has received limited attention in literature. Previous works on transportation resilience utilize only travel delays as the basis for resilience quantification [18], [29], [30]. Existing research on EV resilience primarily focuses on charging station-level metrics such as utilization or trip completion [35], [37], which can miss the effects that the complex interplay between detours, congestion and charging station selection have on total trip delays. Hence, the present research applied OD-pair-level resilience metrics that take into account all major delay dimensions of electrified transportation (travel, charging, and queueing) through a modeling framework that links traffic assignment outputs to delays simulations at the charging station-level. These performance measures are made tractable through their explicit modeling in a coupled workflow, rather than being implicitly included in e.g., topological metrics [36].

The proposed methodology captures several mechanisms by which the individual performance dimensions are affected.

Travel time may increase from necessary alterations to path choice due to disruptions in the network, causing longer travel distances and in turn delays (e.g. OD-pair 37-17 – scenario 1). Additionally, it may be affected by an increase in link congestion as vehicle streams are rerouted, raising travel times (e.g. OD-pair 52-35 – scenario 1) and potentially driving changes in route choice for a certain fraction of vehicles.

Charging times for EV travelers may increase in the mean due to (i) higher energy demands (e.g. from detours or reduced starting SOC, as seen in OD-pair 4-37 – scenario 1) and (ii) reduced effective charging power[8]. The latter may result as an emergent effect of adaptive route-choice behavior to disrupted conditions. Alternatively, it may be caused by increased utilization at charging station locations with heterogeneous EVSE. Here, increased charging demand raises the probability of high-power EVSE being fully occupied, making it more likely for EVs to be assigned to lower-power EVSE, which increases the mean charging time. This mechanism is conditional on the charging demand and the heterogeneity of present EVSE, since it requires utilization changes to shift a charging station from low-utilization regime, where high-power EVSE primarily charge EVs, to a high-utilization regime, where lower-power EVSE supplements supply.

---

[8] This mechanism was not observed in the case study, but is briefly discussed in Section 7.4

Queueing delays are an emergent behavior of charging time and flows through charging station demand $\left[\frac{kWh}{h}\right]$, which in turn may increase through increased vehicle flow or increased energy demands. Additionally, if the total charging power of a charging station location is diminished (e.g. due to vandalism, or power outages – see below) the queue delays also increase.

These mechanisms enable the inference of system properties based on the resilience and performance metrics. For instance, for our baseline EV fleet fraction of $\gamma = 4.52\%$ in scenario 1, the network's loading does not measurably strain the capacities of charging stations, despite choosing peak-hour travel demands and reduced EV ranges (battery capacity and energy consumption, starting SOC). The queueing times represent a negligible component of total delays in both the baseline and disrupted state (as in Fig. 10). The results further show that charging and travel delays are notably increased. Travel delays moderately increased for some OD-pairs, whose path sets are directly affected by the disruption. Hence, recharging EVs and NRVs were delayed to similar extents ($\hat{R}_{tt}^{rs} \approx 1$, for e.g. 37-17), indicating that travel delays are not driven by route choice behavior specific to EVs, but instead by detours and congestion. Further, increased travel delays in indirectly affected paths (e.g. OD-pair 52-35) increased despite retaining identical path sets between network states.

In summary, the disaggregation of resilience metrics allows for systematic and defensible identification of the sources of resilience challenges, and the development of solutions that can improve transportation system resilience in sum (see Section 7.4).

7.3. Discussion of ratio-based resilience metric interpretation

This work chooses to employ ratio-based resilience metrics. Such metrics are conventionally used for resilience assessments for their ease of interpretation as retained level of performance

[22], [29]. However, because these metrics represent resilience in relative terms to the performance level at baseline, their values are influenced by the magnitude of the chosen performance metric at baseline.

This introduces challenges in interpretation using temporal performance metrics, as the same absolute change in delays between OD-pairs can appear overstated in OD-pairs with shorter delays at baseline. This effect overrepresents shorter trips in subsets of highly affected OD-pairs, as well as drives the challenges in evaluating queueing resilience in low utilization regimes.

7.4. Intervention Evaluation

The results of the case study scenario 2 show that the high-power charging capacity at node 37 is pivotal for the network's resilience performance. Loss of the node's charging station location significantly degrades the resilience performance of OD-pairs departing from the node cluster west of the disrupted road link. This section proposes three network interventions to scenario 2 and assesses their resilience performance as a means of demonstrating the framework's capability to evaluate measures to improve resilience.

To mitigate this limitation, results should be conclusively interpreted under consideration of absolute delay metrics or, as has been done throughout this work (Figs. 12, 15 and 16), by evaluating performance dimensions in terms of their overall contribution to trip delays.

7.4.1. Resilience Interventions

To address the resilience loss observed in scenario 2, three interventions are proposed based on resilience results of Section 6.4 and evaluated.

In intervention 1 (I-1), four (4) L2 (14kW) EVSE are added to node 37. In intervention 2 (I-2), one (1) L3 (50kW) EVSE is added to node 37. These interventions provide low-level charging capabilities that may be facilitated through backup generators to address the loss of accessibility reported in Table 3. The single high-power EVSE added in intervention 2 reduces individual charging times, to enable a comparable service level at node 37 to the baseline state and address the significant increase in charging delays (Fig. 15). However, the single EVSE may be susceptible to queue build-ups. Therefore, the multiple parallel EVSE were added in intervention 1, where the total power output in each alternative is similar (56kW (I-1) vs. 50kW (I-2)). In intervention 3 (I-3) one (1) L3 EVSE is added to link 38-39, as it is the charging station location that accommodates a large fraction of the charging demand originally serviced at node 37 (Fig. 13). All other parameters remain unchanged from scenario 2. Each intervention is then simulated end-to-end using the proposed framework to yield resilience results that provide decision support regarding their impact.

Table 4 shows a set of summary statistics that enable the comparison of the resilience performance of the proposed intervention strategies. It includes the arithmetic mean and median of R_{trip}^{rs}-values over $(r, s) \in W$; the lowest R_{trip}^{rs}-value and the 4th percentile of OD-pairs. The 4th percentile was chosen to characterize the tail because the tail comprises 72 (Table 3) out of the total 1631 demand OD-pairs (~4.4%).

Table 4 Summary Statistics comparing the resilience performance of the networks in the default and modified scenario and interventions added to the modified scenario network

Statistic	**Scenario 1**	**Scenario 2**	**I-1**	**I-2**	**I-3**
Mean R_{trip}	0.996	0.975	0.974	0.963	0.983
Median R_{trip}	1.00	1.00	1.00	1.00	1.00
$\min_{(r,s)\in W}\left(R_{trip}^{rs}\right)$	0.835	0.238	0.200	0.088	0. 411
4th Percentile R_{trip}^{rs}	0.977	0.643	0.650	0.301	0.781
$\Delta\left[\sum_{(r,s)\in W} q_{str}^{rs}\right]$	$0.0\,\frac{veh}{h}$	$0.203\,\frac{veh}{h}$	$0.0\,\frac{veh}{h}$	$0.0\,\frac{veh}{h}$	$0.203\,\frac{veh}{h}$

The results for the mean and median of the alternatives show that, there is little change in the overall resilience performance of the network. The disruption impact remains localized to a small subset of OD-pairs, as demonstrated in the tail metrics.

Out of the three alternatives, intervention 3 yields the largest improvements to the network's level-of-service-based resilience metrics, increasing the trip resilience of the tail metrics (4th percentile) from 0.643 to 0.781 and raising the minimum trip resilience from 0.238 to 0.411. It adds charging capacity at a link that already has EVSE allocated to it, which does not improve accessibility over the modified disruption scenario. The higher-power EVSE added to the link enables reduced charging times, yielding large improvements to the trip resilience tail. The added charging capacity in link 38-39 provides the same number of high-power charging stations as node 37 in intervention 2, yet the interventions perform significantly better due to the additional charging capacity at the location, which reduces the overall utilization in the disrupted state ($\Delta\rho_{38-39}^{(1)} = 0.335$) attenuating queue build up. It should be mentioned that the low utilization at link 38-39 is further driven by the reduced overall charging demand in the node cluster, due to the increased number of stranded EVs. Nevertheless, resilience is heavily degraded compared to scenario 1, as the single added L3 EVSE does not provide sufficient capacity to service all recharging EVs. This pushes the location with a boundary utilization regime[9], where EVs that would otherwise wait in queue (Fig. 16) are serviced at a L2 EVSE. However, the resulting increase in mean charging times is far outweighed by the alternative increase in queueing delays experienced at node 37 in intervention 2. This operational regime is indicated by the effective charging power of 35.3kW at the charging station location (arithmetic mean of assigned EVSE

---

[9] This utilization regime is discussed in Section 7.2 as a potential driver of charging resilience degradation

power for all simulated charging events), showing that a significant number of charge events (~40%) is assigned to L2 (14kW) EVSE, reducing the effective power.

In contrast, intervention 1 yields small benefits, through the restoration of accessibility and small improvements to the 4th percentile of R_{trip}^{rs}-values (0.650), compared to the complete removal of the charging station location in node 37. However, it does not address the drastic reduction in trip time resilience shown by the minimum R_{trip}-values, with $\min_{(r,s)\in W}\left(R_{trip}^{rs}\right)$ degrading slightly. Interventions 1 and 2 improve accessibility to electrified transport, because they retain charging capability at node 37.

Intervention 2 adds one (1) high-power EVSE to the disrupted location at node 37. This makes the location highly attractive, drawing significant charging demand from origins in the cut-off node cluster. This drastically increases the location's utilization in the disrupted state to $\Delta\rho_{37}^{(1)} = 0.952$, driving queueing delays (Fig. 16b).

These findings suggest that care must be taken when adding backup charging capacity during disruption scenarios, as a balance must be struck between the provided capacity, and projected demand at the location given the attractiveness of the location. The single high-power EVSE is not sufficient to service the charging demand of the node cluster, causing queueing delays to outweigh the benefits of the reduced charging delays. This conclusion is illustrated in Fig. 16, which shows the component-level breakdown of trip delays for the same OD-pairs shown in Fig. 15 for each proposed intervention.

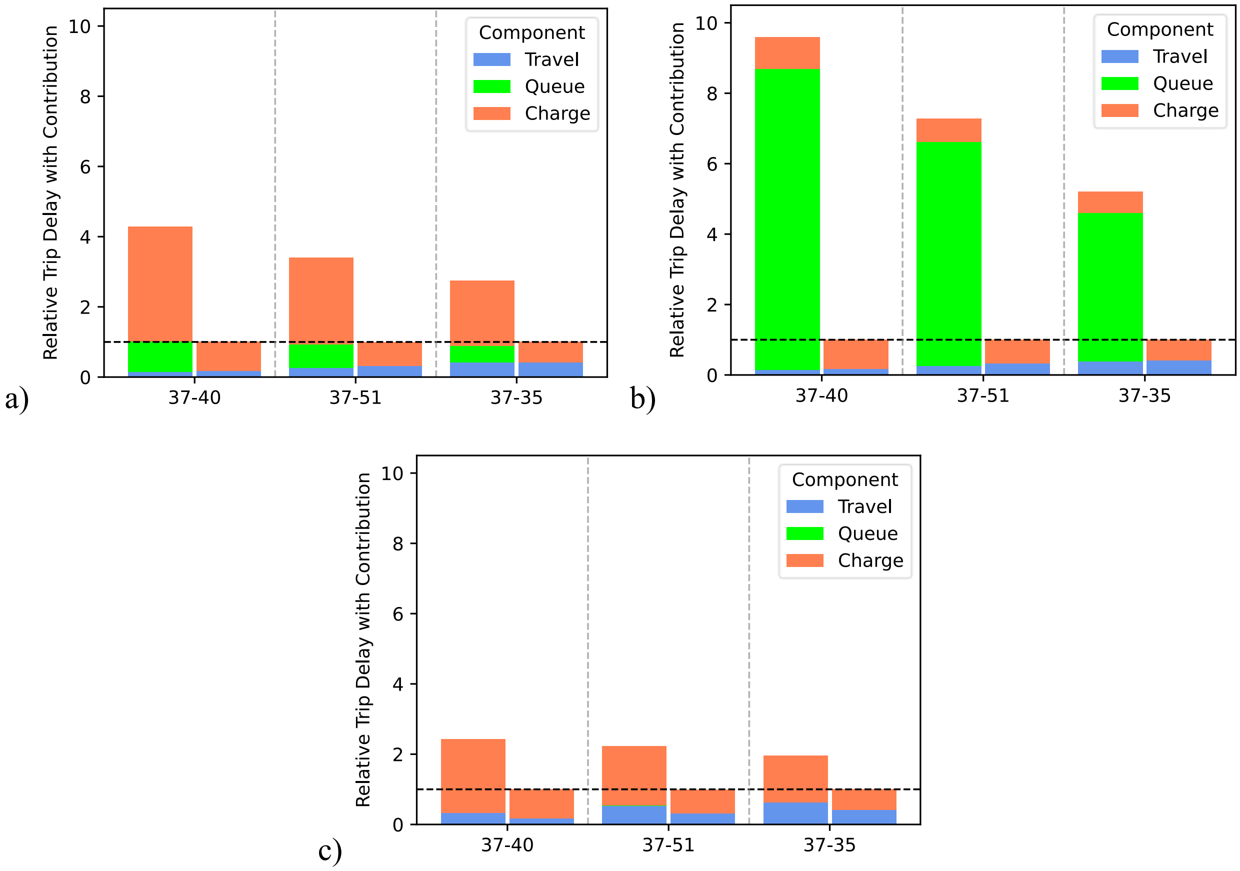

Figure 16 Performance Metric-level decomposition of trip resilience values for the OD-pairs shown in Fig. 15. a) Intervention 1, b) Intervention 2, and c) Intervention 3

The figures show that the queueing delays are the primary driver behind the degraded performance of Intervention 2. The difference in performance between interventions 1 and 3 is less pronounced. However, it is obvious that Intervention 1 exhibits significantly increased queueing as well as charging delays in the disrupted state, with the latter being driven by the difference in effective charging power. This improvement in level-of-service performance comes at the expense of accessibility to the electrified transportation system. Such findings serve as valuable decision-support and should be carefully considered in the context of trade-off analyses.

7.5. Limitations

In the proposed framework, several assumptions were made to simplify the model and make its results more tractable and interpretable. These modeling choices introduce uncertainty and limit the spatial and temporal scope over which the framework is applicable. The following section contains an in-depth discussion of the three highest-impact model limitations, with a comprehensive list of assumptions and their impacts shown in the Appendix A2.

First, the model limits charging station arrivals to the enroute recharging of EVs derived from the TAP. However, a significant proportion of charge events are destination charge events, where the charge event is coincident with and conducted during an extended dwell time at one's destination [43]. This assumption may introduce an underestimation of charging demand at charging stations that coincide with large destination-TAZs, which may cause an underestimation of charging station utilization and, thereby, associated delay metrics. To address this limitation, additional path flows can be added into the data pipeline, that correspond to a fraction of non-recharging EV flow into either end node of a charging station link. The energy demand of each path flow, then, corresponds to the difference between starting energy and the energy required to travel a given path.

Second, the simplification of modeling discrete steady-state network operations limits the framework's application to disruptions whose durations are materially longer than traffic transients and queueing dynamics. Awareness of this limitation is particularly crucial for high-congestion regimes, as it does not allow for carrying over queueing states and the simulation of queue resolution across network states. This may cause underestimation of all delays, but it is particularly relevant to the queueing model, as transient effects are longer than those of road traffic. This limitation can be addressed by restructuring the Monte Carlo simulation framework to model the entire simulation time horizon of a charging station location, such that arrival and energy parameters vary with the simulation time according to the TAP results at each timestep.

Lastly, the proposed model framework has unidirectional coupling that feeds TAP results into the queueing simulation. This structure does not accommodate non-linear charging behaviors such as EVSE shopping or balking[10]. Through the aggregation of EVSE along links, these behaviors can be locally simulated by the queueing mechanisms of the Monte Carlo simulation. However, travel between different charging station locations is omitted, enabling overutilization of charging stations. In the case study presented in Section 6, this limitation has limited impact, as queueing delays are negligible compared to travel and charging delays (Fig. 12). However, as charging station utilization across the network approaches saturation (e.g., in I-2, Section 7.4), the limitation may introduce inaccurate modeling results in that vehicle flows contributing to overutilized charging stations are not redirected to nearby alternatives. This overstates the utilization of highly utilized charging station locations, while underestimating the spread of utilization of charging station locations in its neighborhood, likely skewing the resilience results into two categories, that underestimate the resilience of the highly utilized links and overestimates that of the links in its vicinity.

7.6. Future Work

Future work to address the following key limitations of the proposed framework should focus on including (i) balking into the behavioral model and (ii) destination charging demand.

---

[10] „EVSE shopping“ involves driving by closely located charging stations to derive information on charging queues. “EVSE balking” involves the abandonment of an initial charging station choice upon arrival, for example in case there is a long queue

The first limitation can be addressed by incorporating a flow diversion criterion for charging station links, such that a fraction of the arriving flow is redirected to an alternative charging station link when congestion exceeds a specified threshold. The expected delay at a charging station can be approximated through a closed form queueing model (e.g. M/M/c approximation), using the utilization from Eq. (32). The fraction of diverted flows can, then, be determined by considering every path of a charging station link and computing the redirected flow to the lowest delay alternative such that an equilibrium between the queueing and alternative delay is achieved. Implementing this diversion into the framework would require an iterative feedback loop between the TAP and queueing simulation, or an extending the TAP formulation by a utilization-based penalty term that approximates queueing awareness.

As discussed in the previous section, destination charging can be implemented in the model as a charging station location-specific background flow. This flow could be modeled as a specified fraction of EV flows into the end nodes of a charging station link. The energy demands of these flows can be modeled as the arrival SOC of a given path. This extension would enable more realistic delay estimates for charging station locations in destination-heavy TAZs.

8. Summary and Conclusion

In this research, a methodology for the resilience assessment of electrified transportation is developed to account for travel, charging, and queueing delays. The framework couples an energy-constrained traffic assignment model with a queueing simulation of charging station locations to produce OD-pair-level resilience metrics. These metrics are both interpretable and diagnostic, enabling the decomposition of trip time resilience into its underlying performance dimensions rather than relying aggregated indicator metrics.

The methodology is applied to a case study of a wildfire in Northern Colorado, with results showing that the disruption has uneven impacts across OD-pairs (Figs. 11 & 14 and Table 2). Decomposition of the trip delays further provides insights into the performance loss mechanisms, such as: (i) changes in travel delays from increased road congestion and detours; (ii) increases in charging delays due to shifts in EVSE assignment at locations with heterogeneous EVSE as higher power chargers become occupied; and (iii) emergent growth in queueing delays with increasing utilization of charging station locations. Analysis of system interventions shows that charging station utilization and corresponding delays are shaped by network effects, where adding capacity to charging station links can redistribute flows such that materially different utilization patterns and thereby resilience outcomes are achieved.

These findings underscore the utility of assessing the resilience of electrified transportation systems at an OD-pair-level and decomposing resilience by its performance dimensions. This approach supports diagnosis of the most affected OD-pairs and provides indicators for the mechanisms that drive the performance degradation. The results enable targeted intervention design as well as their evaluation in terms their effects on resilience at both the charging station- and network level.

Results demonstrate that the loss of a single strategically located charging station location can produce severe localized resilience impacts. This loss cannot be mitigated through the addition of high-power backup capacity at the same location, as its benefits can be negated through induced queueing. The findings yield direct implications for the siting of electrified transportation infrastructure in hazard-prone regions. Resilience requires not only the preservation of charging service levels (power) but its geographic distribution and capacity under resilience conditions.

As EV adoption accelerates and climate change-driven disruptions intensify, the proposed methodology provides a tractable tool for planners and policymakers to identify, quantify and mitigate the most critical vulnerabilities of electrified transportation systems before disruptions occur.

References

[1] W. H. Ip and D. Wang, “Resilience and Friability of Transportation Networks: Evaluation, Analysis and Optimization,” *IEEE Syst. J.*, vol. 5, no. 2, pp. 189–198, Jun. 2011, doi: 10.1109/JSYST.2010.2096670.

[2] D. S. Mileti, *Disasters by design: a reassessment of natural hazards in the United States*. Washington, D.C.: Joseph Henry Press, 1999.

[3] E. Hollnagel, D. D. Woods, and N. Leveson, *Resilience Engineering: Concepts and Precepts*, 1st ed. London: CRC Press, 2006.

[4] PIARC Technical Committee 3.3, “Measures for Improving Resilience of Road Network – A PIARC Technical Report,” PIARC (World Road Association), Paris, France, Road Assets Management 2023R38EN, 2023. [Online]. Available: https://www.piarc.org/en/order-library/43543-en-Measures%20for%20Improving%20Resilience%20of%20Road%20Network%20-%20Technical%20Report

[5] T. McDaniels, S. Chang, K. Peterson, J. Mikawoz, and D. Reed, “Empirical Framework for Characterizing Infrastructure Failure Interdependencies,” *J. Infrastruct. Syst.*, vol. 13, no. 3, pp. 175–184, Sep. 2007, doi: 10.1061/(ASCE)1076-0342(2007)13:3(175).

[6] O. Cardona *et al.*, “Determinants of risk: exposure and vulnerability,” in *Managing the Risks of Extreme Events and Disasters to Advance Climate Change Adaptation*, Cambridge, UK and New York, NY, USA: Cambridge University Press, 2012, pp. 65–108.

[7] The White House, *Presidential Policy Directive 21: Critical Infrastructure Security and Resilience*. 2013. [Online]. Available: https://obamawhitehouse.archives.gov/the-press-office/2013/02/12/presidential-policy-directive-critical-infrastructure-security-and-resil

[8] Q. Li, S. Soleimaniamiri, and X. Li, “Optimal mass evacuation planning for electric vehicles before natural disasters,” *Transp. Res. Part Transp. Environ.*, vol. 107, p. 103292, Jun. 2022, doi: 10.1016/j.trd.2022.103292.

[9] K. Tierney, “Foreshadowing Katrina: Recent Sociological Contributions to Vulnerability Science,” *Contemp. Sociol. J. Rev.*, vol. 35, no. 3, pp. 207–212, May 2006, doi: 10.1177/009430610603500302.

[10] S. L. Cutter, R. L. Schumann, and C. T. Emrich, “Exposure, Social Vulnerability and Recovery Disparities in New Jersey after Hurricane Sandy,” *J. Extreme Events*, vol. 01, no. 01, p. 1450002, Aug. 2014, doi: 10.1142/S234573761450002X.

[11] C. S. Holling, “Resilience and Stability of Ecological Systems,” *Annu. Rev. Ecol. Syst.*, vol. 4, no. 1, pp. 1–23, Nov. 1973, doi: 10.1146/annurev.es.04.110173.000245.

[12] N. A. of Engineering, *Engineering Within Ecological Constraints*. Washington, DC: The National Academies Press, 1996. doi: 10.17226/4919.

[13] P. Murray-tuite, “A Comparison of Transportation Network Resilience under Simulated System Optimum and User Equilibrium Conditions,” in *Proceedings of the 2006 Winter Simulation Conference*, Monterey, CA, USA: IEEE, Dec. 2006, pp. 1398–1405. doi: 10.1109/WSC.2006.323240.

[14] M. Bruneau *et al.*, “A Framework to Quantitatively Assess and Enhance the Seismic Resilience of Communities,” *Earthq. Spectra*, vol. 19, no. 4, pp. 733–752, Nov. 2003, doi: 10.1193/1.1623497.

[15] Colorado Department of Transportation, “4R Framework for Identifying and Evaluating Resiliency in Transportation System Assets and Organizations.” 2024. [Online]. Available: https://www.codot.gov/programs/planning/assets/risk-and-resiliency/4r-framework-remediated.pdf

[16] P. Bocchini and D. M. Frangopol, “Restoration of Bridge Networks after an Earthquake: Multicriteria Intervention Optimization,” *Earthq. Spectra*, vol. 28, no. 2, pp. 427–455, May 2012, doi: 10.1193/1.4000019.

[17] Y. Wang, H. Liu, K. Han, T. L. Friesz, and T. Yao, “Day-to-day congestion pricing and network resilience,” *Transp. Transp. Sci.*, vol. 11, no. 9, pp. 873–895, Oct. 2015, doi: 10.1080/23249935.2015.1087234.

[18] R. Twumasi-Boakye and J. O. Sobanjo, “Resilience of Regional Transportation Networks Subjected to Hazard-Induced Bridge Damages,” *J. Transp. Eng. Part Syst.*, vol. 144, no. 10, p. 04018062, Oct. 2018, doi: 10.1061/JTEPBS.0000186.

[19] Y. Zhou, J. Wang, and H. Yang, “Resilience of Transportation Systems: Concepts and Comprehensive Review,” *IEEE Trans. Intell. Transp. Syst.*, vol. 20, no. 12, pp. 4262–4276, Dec. 2019, doi: 10.1109/TITS.2018.2883766.

[20] S. E. Chang and M. Shinozuka, “Measuring Improvements in the Disaster Resilience of Communities,” *Earthq. Spectra*, vol. 20, no. 3, pp. 739–755, Aug. 2004, doi: 10.1193/1.1775796.

[21] G. P. Cimellaro, C. Renschler, A. M. Reinhorn, and L. Arendt, “PEOPLES: A Framework for Evaluating Resilience,” *J. Struct. Eng.*, vol. 142, no. 10, p. 04016063, Oct. 2016, doi: 10.1061/(ASCE)ST.1943-541X.0001514.

[22] D. A. Reed, K. C. Kapur, and R. D. Christie, “Methodology for Assessing the Resilience of Networked Infrastructure,” *IEEE Syst. J.*, vol. 3, no. 2, pp. 174–180, Jun. 2009, doi: 10.1109/JSYST.2009.2017396.

[23] B. Berche, C. Von Ferber, T. Holovatch, and Yu. Holovatch, “Resilience of public transport networks against attacks,” *Eur. Phys. J. B*, vol. 71, no. 1, pp. 125–137, Sep. 2009, doi: 10.1140/epjb/e2009-00291-3.

[24] A. A. Ganin, M. Kitsak, D. Marchese, J. M. Keisler, T. Seager, and I. Linkov, “Resilience and efficiency in transportation networks,” *Sci. Adv.*, vol. 3, no. 12, p. e1701079, Dec. 2017, doi: 10.1126/sciadv.1701079.

[25] Z. Xu, S. S. Chopra, and H. Lee, “Resilient Urban Public Transportation Infrastructure: A Comparison of Five Flow-Weighted Metro Networks in Terms of the Resilience Cycle Framework,” *IEEE Trans. Intell. Transp. Syst.*, vol. 23, no. 8, pp. 12688–12699, Aug. 2022, doi: 10.1109/TITS.2021.3116667.

[26] E. Miller-Hooks, X. Zhang, and R. Faturechi, “Measuring and maximizing resilience of freight transportation networks,” *Comput. Oper. Res.*, vol. 39, no. 7, pp. 1633–1643, Jul. 2012, doi: 10.1016/j.cor.2011.09.017.

[27] D. Freckleton, K. Heaslip, W. Louisell, and J. Collura, “Evaluation of Resiliency of Transportation Networks after Disasters,” *Transp. Res. Rec. J. Transp. Res. Board*, vol. 2284, no. 1, pp. 109–116, Jan. 2012, doi: 10.3141/2284-13.

[28] N. U. Serulle, K. Heaslip, B. Brady, W. C. Louisell, and J. Collura, “Resiliency of Transportation Network of Santo Domingo, Dominican Republic: Case Study,” *Transp. Res. Rec. J. Transp. Res. Board*, vol. 2234, no. 1, pp. 22–30, Jan. 2011, doi: 10.3141/2234-03.

[29] M. Omer, A. Mostashari, and R. Nilchiani, “Assessing resilience in a regional road-based transportation network,” *Int. J. Ind. Syst. Eng.*, vol. 13, no. 4, p. 389, 2013, doi: 10.1504/IJISE.2013.052605.

[30] B. K. Bhavathrathan and G. R. Patil, “Capacity uncertainty on urban road networks: A critical state and its applicability in resilience quantification,” *Comput. Environ. Urban Syst.*, vol. 54, pp. 108–118, Nov. 2015, doi: 10.1016/j.compenvurbsys.2015.07.005.

[31] R. Faturechi and E. Miller-Hooks, “A Mathematical Framework for Quantifying and Optimizing Protective Actions for Civil Infrastructure Systems,” *Comput.-Aided Civ. Infrastruct. Eng.*, vol. 29, no. 8, pp. 572–589, Sep. 2014, doi: 10.1111/mice.12027.

[32] M. Nogal, A. O’Connor, B. Martinez-Pastor, and B. Caulfield, “Novel Probabilistic Resilience Assessment Framework of Transportation Networks against Extreme Weather Events,” *ASCE-ASME J. Risk Uncertain. Eng. Syst. Part Civ. Eng.*, vol. 3, no. 3, p. 04017004, Sep. 2017, doi: 10.1061/AJRUA6.0000908.

[33] Q. Zhang, H. Yu, G. Zhang, and T. Ma, “Optimal planning of flood-resilient electric vehicle charging stations,” *Comput.-Aided Civ. Infrastruct. Eng.*, vol. 38, no. 4, pp. 489–507, Mar. 2023, doi: 10.1111/mice.12853.

[34] A. Hussain and H.-M. Kim, "Evaluation of Multi-Objective Optimization Techniques for Resilience Enhancement of Electric Vehicles," *Electronics*, vol. 10, no. 23, p. 3030, Dec. 2021, doi: 10.3390/electronics10233030.

[35] G. Raman, G. Raman, and J. C.-H. Peng, "Resilience of urban public electric vehicle charging infrastructure to flooding," *Nat. Commun.*, vol. 13, no. 1, p. 3213, Jun. 2022, doi: 10.1038/s41467-022-30848-w.

[36] O. F. Hamim, X. Chen, and S. V. Ukkusuri, "Developing a framework for resilience assessment of electric vehicle charging station networks," *J. Transp. Geogr.*, vol. 128, p. 104349, Oct. 2025, doi: 10.1016/j.jtrangeo.2025.104349.

[37] H. Wang, A. F. Abdin, Y. Fang, and E. Zio, "Resilience assessment of electrified road networks subject to charging station failures," *Comput.-Aided Civ. Infrastruct. Eng.*, vol. 37, no. 3, pp. 300–316, Mar. 2022, doi: 10.1111/mice.12736.

[38] Z. Zhang, W. Hao, Y. Gong, W. Wu, Y. Chen, and S. Lu, "Impact of Electric Vehicles on Traffic Assignment and Carbon Emission for Road Network: Modeling and Analysis," *J. Adv. Transp.*, vol. 2025, no. 1, p. 8640594, Jan. 2025, doi: 10.1155/atr/8640594.

[39] Z. Liang *et al.*, "A Strategic EV Charging Networks Planning Framework for Intercity Highway With Time-Expanded User Equilibrium," *IEEE Trans. Smart Grid*, vol. 16, no. 6, pp. 5215–5229, Nov. 2025, doi: 10.1109/TSG.2025.3587258.

[40] H. Liu and D. Z. W. Wang, "Locating multiple types of charging facilities for battery electric vehicles," *Transp. Res. Part B Methodol.*, vol. 103, pp. 30–55, Sep. 2017, doi: 10.1016/j.trb.2017.01.005.

[41] Y.-G. Lee, H.-S. Kim, S.-Y. Kho, and C. Lee, "User Equilibrium–Based Location Model of Rapid Charging Stations for Electric Vehicles with Batteries that have Different States of Charge," *Transp. Res. Rec. J. Transp. Res. Board*, vol. 2454, no. 1, pp. 97–106, Jan. 2014, doi: 10.3141/2454-13.

[42] K. Liu and Y. Liu, "Stochastic user equilibrium based spatial-temporal distribution prediction of electric vehicle charging load," *Appl. Energy*, vol. 339, p. 120943, Jun. 2023, doi: 10.1016/j.apenergy.2023.120943.

[43] A. I. Rabinowitz, J. G. Smart, T. C. Coburn, and T. H. Bradley, "A Geo-Spatial Method for Calculating BEV Charging Inconvenience using Publicly Available Data," *INSIGHT*, vol. 27, no. 1, pp. 27–38, Feb. 2024, doi: 10.1002/inst.12473.

[44] J. G. Wardrop, "Some Theoretical Aspects of Road Traffic Research," *Proc. Inst. Civ. Eng.*, vol. 1, no. 3, pp. 325–362, May 1952, doi: 10.1680/ipeds.1952.11259.

[45] J. E. Anderson, M. Bergfeld, D. M. Nguyen, and F. Steck, “Real-world charging behavior and preferences of electric vehicles users in Germany,” *Int. J. Sustain. Transp.*, vol. 17, no. 9, pp. 1032–1046, Sep. 2023, doi: 10.1080/15568318.2022.2147041.

[46] A. A. Visaria, A. F. Jensen, M. Thorhauge, and S. E. Mabit, “User preferences for EV charging, pricing schemes, and charging infrastructure,” *Transp. Res. Part Policy Pract.*, vol. 165, pp. 120–143, Nov. 2022, doi: 10.1016/j.tra.2022.08.013.

[47] G. Ferro, R. Minciardi, and M. Robba, “A user equilibrium model for electric vehicles: Joint traffic and energy demand assignment,” *Energy*, vol. 198, p. 117299, May 2020, doi: 10.1016/j.energy.2020.117299.

[48] Z. Zhou, H. Sun, and Q. Guo, “Stochastic User Equilibrium in Charging Station Selection Based on Discrete Choice Model,” in *2018 IEEE Power & Energy Society General Meeting (PESGM)*, Portland, OR: IEEE, Aug. 2018, pp. 1–5. doi: 10.1109/PESGM.2018.8586008.

[49] N. Pearre, N. Jayanath, and L. Swan, “Evaluating Unplug Incentives to Improve User Experience and Increase DC Fast Charger Utilization,” *World Electr. Veh. J.*, vol. 16, no. 11, p. 623, Nov. 2025, doi: 10.3390/wevj16110623.

[50] Y. Sheffi, *Urban transportation networks: equilibrium analysis with mathematical programming methods*. Englewood Cliffs, N.J: Prentice-Hall, 1984.

[51] J. F. C. Kingman, “The first Erlang century—and the next,” *Queueing Syst.*, vol. 63, no. 1–4, pp. 3–12, Dec. 2009, doi: 10.1007/s11134-009-9147-4.

[52] J. F. Shortle, J. M. Thompson, D. Gross, and C. M. Harris, *Fundamentals of Queueing Theory*, 1st ed. in Wiley Series in Probability and Statistics. Wiley, 2018. doi: 10.1002/9781119453765.

[53] Colorado Department of Transportation, “Traffic Analysis and Forecasting Guidelines.” 2023. [Online]. Available: https://www.codot.gov/safety/traffic-safety/assets/traffic_analysis_forecasting_guidelines/traffic_analysis_forecasting_guidelines

[54] National Interagency Fire Center, “NIFC FTP Server - Incident Specific Data.” [Online]. Available: https://ftp.wildfire.gov/

[55] Colorado Department of Transportation, “US 34 in Big Thompson Canyon closed to allow for evacuations of residents due to Cameron Peak fire escalation.” [Online]. Available: https://www.codot.gov/news/2020/october-2020/us34-firerelatedclosure

[56] Colorado Department of Transportation, “Highway Data Explorer — OTIS Online Transportation Information System.” [Online]. Available: https://dtdapps.coloradodot.info/otis/HighwayData

[57] Transportation Research Board, *Highway Capacity Manual*, 4. ed., Metric units version. in Highway capacity manual / Transportation Research Board, no. 2000. Washington, DC: TRB, 2000.

[58] Vehicle Technologies Office, “Enabling Extreme Fast Charging: A Technology Gap Assessment,” U.S. Department of Energy, Oct. 2017. [Online]. Available: https://www.energy.gov/eere/vehicles/articles/enabling-extreme-fast-charging-technology-gap-assessment

[59] Kumar, Himangshu, “EValuateCO – vehicle electrification dashboard for Colorado,” Atlas Public Policy. [Online]. Available: https://atlaspolicy.com/evaluateco

[60] K. A. Small, E. T. Verhoef, and R. Lindsey, *The economics of urban transportation*, Third edition. Abingdon, Oxon ; New York, NY: Routledge, Taylor & Francis Group, 2024.

[61] S. Kyle, “What we know Monday: Cameron Peak evacuation for Big Thompson Canyon lifted,” Coloradoan. [Online]. Available: https://www.coloradoan.com/story/news/2020/10/19/cameron-peak-fire-live-coverage-monday-what-we-know-fire/3706158001/

Appendix

A1. Traffic Assignment Problem (TAP) solution algorithm

This section summarizes the numerical procedures used to solve the proposed constrained nonlinear optimization program (NLP). The TAP is formulated as a path-based convex optimization problem with two vehicle classes: non-recharging vehicles ($m = 1$) and recharging EVs ($m = 2$). The convex program is solved using MATLAB's constrained optimizer (fmincon, interior-point).

Because the path flows are the optimization variables, the algorithm may require full path enumeration to converge to a global optimum of the path-based convex program. This approach is very computationally expensive. Therefore, the MATLAB solver is nested in a column generation (CG) algorithm, which iteratively adds paths to path sets, where a new, fastest path could be determined. This approach ensures a full path set at the global solution, while lowering computational costs.

A1.1. TAP Solution Algorithm

Figure A-1, summarizes the solution algorithm used to solve the TAP for a given set of path sets. It is solved separately for each network state using a path-based convex program with two vehicle classes. The solution produces equilibrium path flows and link flows, path travel times, and recharging EV charging demands at charging station links.

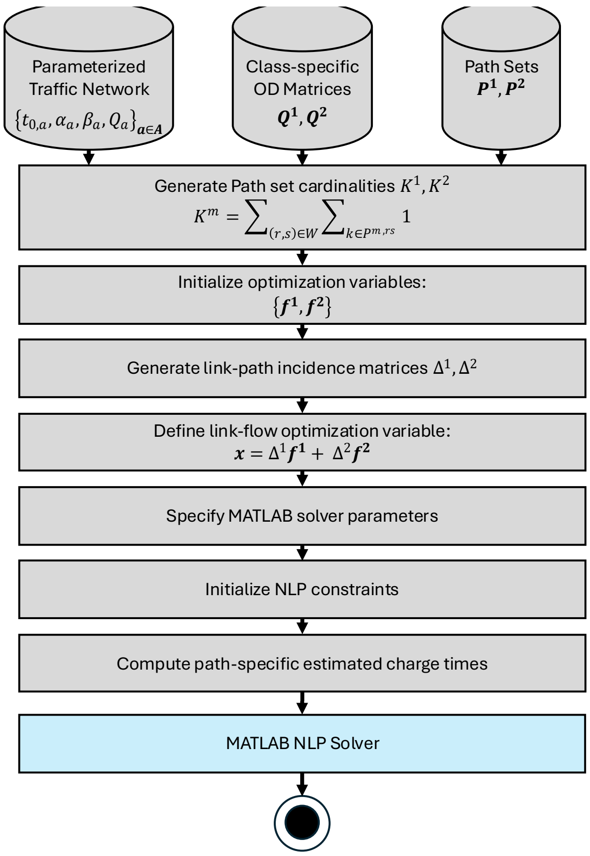

Figure A-1 Flow Chart of the TAP solution algorithm

The modeled electrified transportation systems is represented by a directed network graph $G = (N, A)$ with link free-flow times $t_{0,a}$, capacities Q_a, and delay characteristic parameters α_a and β_a, as well as a subset of charging station links $\tilde{A} \subseteq A$, with charging station location attributes: expected output power $P_{\tilde{a}}$. The travel demands of each vehicle class ($m = \{1,2\}$) are specified through class-specific OD-matrices, which are assigned to path sets, $\boldsymbol{P^1}$ and $\boldsymbol{P^2}$.

Given the path set of each OD pair $P^{m,rs} \in \boldsymbol{P^m}$, $\forall m \in M, (r,s) \in W$, the total number of total number of paths for a given vehicle class, K^m, is determined using:

$$K^m = \sum_{(r,s)\in W} \sum_{k\in P^{m,rs}} 1.$$

Using these, the path flow optimization variables, $\boldsymbol{f^1}$ and $\boldsymbol{f^2}$, are initialized as vectors of size $K^m \times 1$. Through the path sets and list of network links, the link-path incidence matrices Δ^1 and

Δ^2 are computed, where each row corresponds to the binary values $\delta_{a,k}^{m,rs}$ which encode whether the link $a \in A$ is an element of the path $k \in P^{m,rs}$. These enable the definition of the link flow vector optimization variable required to define the objective function Eq. (16), as:

$$\boldsymbol{x} = \Delta^1 \boldsymbol{f}^{\mathbf{1}} + \Delta^2 \boldsymbol{f}^{\mathbf{2}}.$$

The optimization problem objective in MATLAB is defined through the instantiation of an optimization-options objects, which specifies the solution algorithm (interior-point), subproblem algorithm (factorization), convergence tolerances, and maximum number of iterations. Additionally, the matrices to define linear constraints (A_{eq}, b_{eq}), nonlinear constraints (A_{ineq}, b_{ineq}) and upper and lower bounds of optimization variables (lb, ub) are specified, such that:

$$\min_{\mathbf{y}} f(\boldsymbol{y})$$

s.t.

$$\boldsymbol{A_{eq}} \boldsymbol{y} = \boldsymbol{b_{eq}}$$

$$\boldsymbol{A_{ineq}} \boldsymbol{y} \leq \boldsymbol{b_{ineq}}$$

$$\boldsymbol{lb} \leq \boldsymbol{y} \leq \boldsymbol{ub}$$

To define the objective function, path specific generalized charging costs, $\boldsymbol{c}^{\mathbf{2}}$, are computed using Eq. (11). The objective function is then initialized as:

$$Z(\boldsymbol{f}) = \sum_{a \in A} \left[t_{0,a} x_a + t_{0,a} \frac{\alpha_a}{\beta_a + 1} \frac{x_a^{\beta_a + 1}}{Q^{\beta_a}} \right] + [\boldsymbol{c}^{\mathbf{2}}]^{\boldsymbol{T}} \boldsymbol{f},$$

where $\boldsymbol{f} = [\boldsymbol{f}^{\mathbf{1}};\ \boldsymbol{f}^{\mathbf{2}}]$. The fully initialized convex constrained program is solved using MATLAB's fmincon (interior-point) function. Solver options specify the algorithm, subproblem strategy (factorization), maximum iterations, and convergence tolerances.

A1.2. Column Generation Algorithm

The TAP optimization program is executed within an outer Column Generation (CG) algorithm, which iteratively adds paths to path sets, if, at a given traffic assignment, a new, lower cost path can be found. The CG algorithm initializes with minimal path sets. In a realistic network, this necessitates several iterations to populate the path sets and arrive at a global solution. Therefore, the algorithm operates in two stages. The first stage has relaxed convergence criteria parameters:

$$\epsilon_{opt,1} = 10^{-5}, \epsilon_{const,1} = 10^{-8}, \epsilon_{step,1} = 10^{-10}, \qquad MaxIter_1 = 1{,}500,$$

to enable faster convergence and thereby population of path sets. Once the path no better paths can be found, the second stage is initialized, which utilizes tighter convergence criteria:

$$\epsilon_{opt,2} = 10^{-6}, \epsilon_{const,2} = 10^{-10}, \epsilon_{step,2} = 10^{-12}, \qquad MaxIter_2 = 1{,}500,$$

to ensure a more accurate solution.

Figure A-2 shows a flow chart resembling the structure of the CG algorithm. It initializes the minimal path sets. For non-recharging vehicles ($m = 1$) path sets consist of only the lowest delay path using the unloaded network. Recharging vehicles' path sets ($m = 2$) include the path with the generalized cost path as well as the lowest cost, feasible path that incorporates the closest (by distance) charging station location to a given OD-pair's origin. This ensures consistency with the range constraints and the number of stranded EVs, $q_{str}^{2,rs}$. The TAP optimizer's first stage convergence parameters are specified and the CG loop is entered.

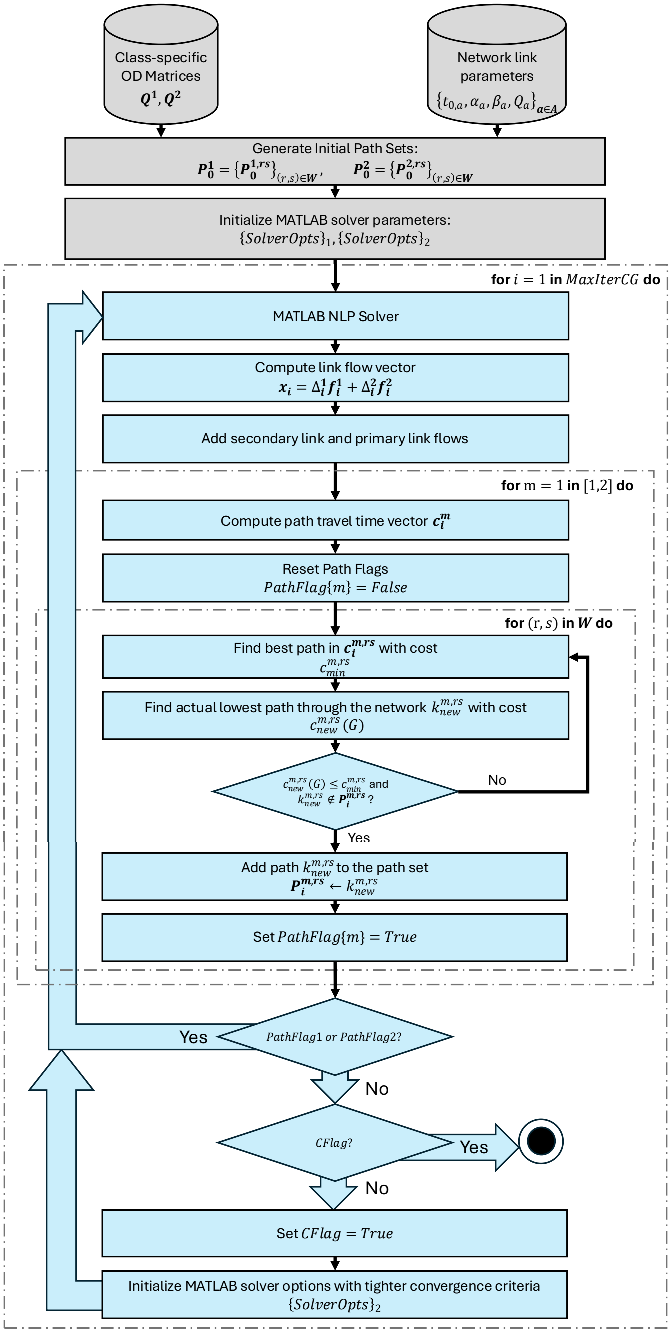

Figure A-2 Flow Chart of CG algorithm with nested nonlinear constrained optimizer

Within the main CG algorithm loop, MATLAB's fmincon function is executed, which yields optimal path flows for the i-th iteration's path sets, $\boldsymbol{P_i^1}$ and $\boldsymbol{P_i^2}$. This is converted to link flows to enable the calculation of path costs and efficient execution of shortest path algorithms. Then, the link flows of primary and secondary links are, again, combined to accurately reflect the actual traffic on a given road segment.

To populate path sets, each OD-pair is checked for improving paths. For non-recharging vehicles, the path cost is calculated as the sum of its link travel times at the CG iteration's network loading. For the lowest travel cost a path set $\boldsymbol{P_i^{1,rs}}$ for $(r,s) \in W$ is then:

$$c_{min}^{1,rs} = \min_{\mathrm{k \in P^{1,rs}}} c_k^{1,rs}.$$

The candidate path that may be added to the path set $k_{new}^{1,rs}$ is the path through the loaded network connecting the OD-pair with the lowest cumulative travel time. If its cost $c_{new}^{1,rs}$ is smaller than or equal to $c_{min}^{1,rs}$ and $k_{new}^{1,rs}$ is not yet contained in $P^{1,rs}$, it is added to the path set.

For recharging EVs ($m = 2$), the range constraints limit the accessibility to charging stations for subsets of the travel demand. Therefore, the fastest path for each subset must be considered. These are demarcated by their reachability thresholds $U_k^{2.rs}$, associated with each path $k \in \boldsymbol{P_i^{2,rs}}$.

A path $k_{new}^{2,rs}$ is added if its generalized cost is lower than that of every path in the path set with a greater reachability threshold. In other words, a path is only added if it has a lower cost than every alternative available to the given subset of recharging EVs capable of reaching it, given their starting SOC. To that end, the candidate path is being compared to:

$$c_{min}^{2,rs}\left(U_{k_{new}}^{2,rs}\right) = \min\left[c_j^{2,rs} \mid j \in \boldsymbol{P_i^{2,rs}}, U_j^{2,rs} \geq U_k^{2,rs}\right].$$

If no new paths were added to *any* set, the algorithm advances to the second stage by setting the tighter convergence criteria for the TAP solution algorithm and setting a flag that the second stage was entered. The algorithm, then, continues its loop, possibly adding new paths, since the tighter convergence criteria yield different path flows. The CG algorithm terminates when (i) the optimizer converges and (ii) no improving paths are found using the second stage's convergence criteria.

A1.2.1. Shortest Path Algorithm

The CG algorithm is heavily reliant on shortest path algorithms to populate path sets and determine convergence. Since non-recharging vehicles ($m = 1$), do not have constraints on their path choices, shortest paths can be found using a common k-shortest path algorithm on a link travel time-weighted network graph.

To determine the best path for a given OD-pair for recharging vehicles ($m = 2$), the cumulative generalized cost of travel and expected charge time must be considered. Since the charging delay is a function of the travel distance to a charging station link, a conventional shortest path algorithm is not sufficient. To determine the path with the lowest cumulative generalized cost, the best path using each charging station location link, $\tilde{a} \in \tilde{A}$, is determined, which enables us to find the lowest cost path that includes any charging station location. Due to their efficiency, it is desirable to leverage shortest path algorithms for finding the lowest cost path for a given charging station link. To this end, paths are separated into two sections, (i) the path-section from the origin node to the charging station link and (ii) the path-section from the charging station link to the trip destination. Since it is assumed that travelers only visit one charging station during their trip, the latter can be found directly through a shortest path algorithm on a link travel time-weighted network. As stated previously, the path to the charging station link, however, impacts the charging delay, due to the travel energy demand that is proportional to its length. Therefore, to determine the lowest cumulative delay path to a charging station link, a temporary graph is created, with the link weights:

$$w_a = c_a(x_a) + \eta \frac{u d_a}{\bar{P}_{\tilde{a}}},$$

where d_a is the length of link $a \in A$, u is the energy consumption of EVs $\left[\frac{kWh}{km}\right]$, η is the VOT-factor for recharging delay relative to driving delays, $c_a(x_a)$ is the travel delay incurred for traveling over the road segment $a \in A$ and $\bar{P}_{\tilde{a}}$ is the expected charging power at the charging station location , $\tilde{a} \in \tilde{A}$, of the path. In other words, the added marginal generalized cost of traveling along a link of length d_a is added to the travel delay link weights. These link-weights enable us to use conventional shortest path algorithms for each path section to determine the minimal cumulative delay path for a given charging station location, $\tilde{a} \in \tilde{A}$.

A2. Limitations

Table A-1 Limitations of the proposed modeling framework, their impacts on simulation results and approaches to mitigate them

Nr.	Limitation	Impact	Mitigation
1	Only consider enroute charging	Underestimate charging station utilization and thereby delays, overestimating resilience	Location-specific TAP-invariant baseline demand on top of enroute demand
2	Discretization into steady network states	Lack of state carryover and simulation of queue resolution may overestimate resilience	Adjust queueing simulation to simulate entire simulation time horizon
3	Unidirectional coupling	No balking overestimates utilization at high utilization links and underestimates utilization at surrounding links. This distorts resilience distributions	Implement diversion criterion at charging station links, where flow pushing delays past a threshold are reassigned to alternative charging stations (Section 7.6)
4	Homogeneous battery size and energy consumption	Inaccurate charging demand distribution compared to real-world may cause distort resilience distributions	
5	Homogeneous VOT across driver population	Skews utilization towards lower or higher power charging stations, depending on choice of η, consequently skewing resilience.	
6	Charging Cost is negligible as choice parameter	Since cost is typically proportional to charger power, flow to high power links may be overestimated, underestimating their resilience and overestimating resilience of lower power alternatives.	Include penalty for charging cost, similar to Ferro et al. [47].

7	Amenities at charging station locations are negligible as choice parameters	Flow distribution may be skewed, skewing resilience distribution.	Include reward (negative penalty) for ordinal amenity score at links.
8	EVs always charge their battery to 80%	May overestimate charging delay and create knock-on queueing delays, underestimating resilience	Monte Carlo simulation can be modified such that charging duration is randomly sampled between an SOC interval.
9	EVs leave EVSE as soon as their vehicle reaches the target SOC	May underestimate charging delay in some instances, where fully charged still occupy EVSE, overestimating resilience.	Similar to 8, randomly sample excess occupation duration until EV is unplugged
10	Effective SOC is 80% of the total battery capacity	May underestimate EV ranges, thereby overestimating charging demand, consequently underestimating resilience	Separate target SOC in queueing simulation from available SOC in TAP
11	Charging demand based on physical route feasibility	Disregarding range anxiety from route feasibility OD demand of vehicle type $m = 2$, underestimating charging demands, thereby overestimating resilience	A fixed offset to the feasibility thresholds (Eq. (14)) may emulate range anxiety

A3. Model Verification and Validation

A3.1. TAP Constraint Violations

Table A-2 Constraint violations of the TAP solutions for the case study scenarios

Parameter Set	**Max. Mean constraint violation (violating const.)**	**Max Constraint violation (violating const.)**
Scenario 1		
$\{\boldsymbol{\alpha}^r = \mathbf{1.5}, \boldsymbol{\beta}^r = \mathbf{1.0}, \boldsymbol{\gamma}^r = \mathbf{0.0452}\}_{\forall \boldsymbol{r} \in \boldsymbol{N}}$, $\boldsymbol{\eta} = \mathbf{2.0}, \boldsymbol{u} = \mathbf{0.2175}, \boldsymbol{disrupted} = \boldsymbol{false}$	$1.61 \cdot 10^{-14}$ (flow cons.)	$1.49 \cdot 10^{-11}$ (flow cons.)
$\{\boldsymbol{\alpha}^r = \mathbf{1.5}, \boldsymbol{\beta}^r = \mathbf{1.0}, \boldsymbol{\gamma}^r = \mathbf{0.0452}\}_{\forall \boldsymbol{r} \in \boldsymbol{N}}$, $\boldsymbol{\eta} = \mathbf{2.0}, \boldsymbol{u} = \mathbf{0.2175}, \boldsymbol{disrupted} = \boldsymbol{true}$	$2.35 \cdot 10^{-11}$ (flow cons.)	$2.62 \cdot 10^{-11}$ (flow cons.)
Scenario 2		
$\{\boldsymbol{\alpha}^r = \mathbf{1.5}, \boldsymbol{\beta}^r = \mathbf{1.0}, \boldsymbol{\gamma}^r = \mathbf{0.0452}\}_{\forall \boldsymbol{r} \in \boldsymbol{N}}$, $\boldsymbol{\eta} = \mathbf{2.0}, \boldsymbol{u} = \mathbf{0.2175}, \boldsymbol{disrupted} = \boldsymbol{true}$	$2.18 \cdot 10^{-11}$ (flow cons.)	$2.58 \cdot 10^{-11}$ (flow cons.)

The maximum absolute values constraint violations are $< 3 \cdot 10^{-11}$, indicating that the algorithm implementation produces feasible solutions. Every maximum constraints violation was committed by the flow conservation constraints, where the other constraints (nonnegativity and range constraint) exhibited smaller violation values.

A3.2. Monte Carlo Simulation Stability

A3.2.1. Stability

To establish the numerical stability of the Monte Carlo simulation results, the simulation is executed 10 times for the parameter set:

$$\{\alpha^r = 1.5, \beta^r = 1.0, \gamma^r = 0.0452\}_{\forall r \in N},$$
$$\eta = 2.0, \qquad u = 0.2175, \qquad disrupted = true,$$

using $n_{MC} = 500{,}000$ and $1{,}000{,}000$, with $w = 0$. Using the set of simulation results, validation metrics for charging and queueing delays of each OD-pair are calculated to determine whether n_{MC} is sufficiently large to enable sufficiently small uncertainties. The results for charging delays are reported as relative halfwidth, $\frac{h}{\bar{c}_c}$ of a given OD-pair $(r, s) \in W$:

$$\frac{h}{\bar{c}_c} = t_{\frac{\alpha}{2}}[n-1]\frac{s(c_c)}{\sqrt{n}},$$

where $\bar{c}_c$ is the arithmetic mean of the sampled charging delays, $t_{\frac{\alpha}{2}}[n-1]$ is the $1 - \frac{\alpha}{2}$ quantile (here 0.95) of the t-distribution with $n - 1$ degrees of freedom, $s(c_c)$ is the sample standard deviation of the charging delays of an OD-pair and n is the number of samples (here 10).

Because queueing delays can take very small values (see Section 6.3), relative metrics can yield misleading results due to the volatility introduced by small denominators. Therefore, the accuracy of queueing results are reported as absolute halfwidth h of a given OD-pair $(r, s) \in W$:

$$h = t_{\frac{\alpha}{2}}[n-1]\frac{s(c_q)}{\sqrt{n}},$$

where $s(c_q)$ is the sample standard deviation of the charging delays of an OD-pair.

After the 10 Monte Carlo simulations, the halfwidths of queueing delays and relative halfwidth of charging delays are calculated at 90% confidence (two-tailed). The results for $n_{MC} = 500{,}000$

and 1,000,000 are illustrated in Figures A-3 and A-4 as histograms. Fig. A-3 shows the counts of OD-pairs by the relative two-tailed halfwidth of their charging delays logarithmically binned by magnitudes of 10. Fig. A-4 shows the counts of OD-pairs by the two-tailed halfwidth of their queueing delays $[h]$ logarithmically binned by magnitudes of 10.

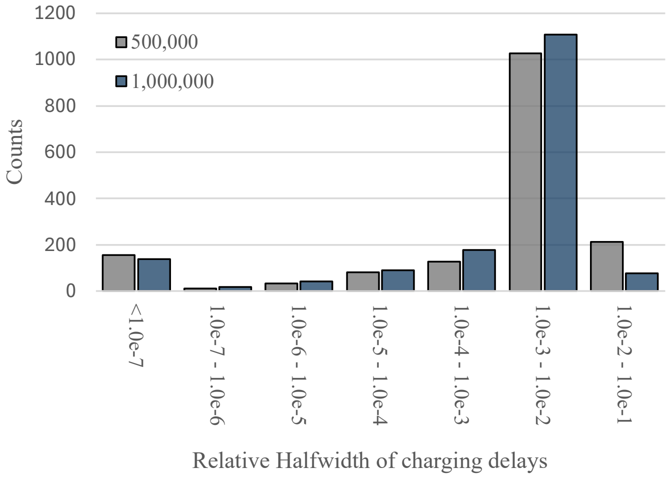

Figure A-3 OD-pair relative halfwidth of charging delays counts with logarithmic (base 10) binning

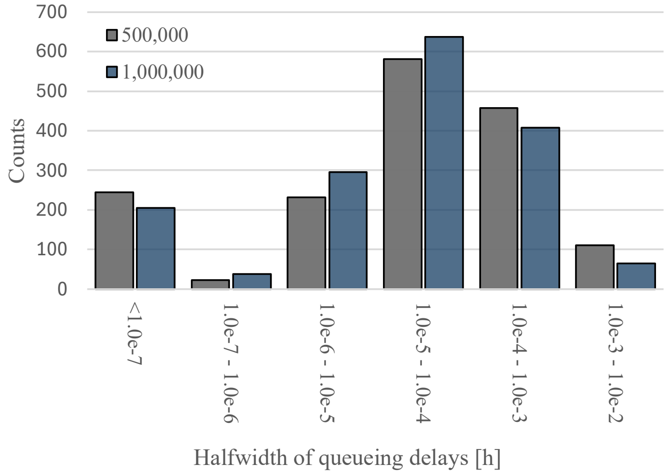

Figure A-4 OD-pair halfwidth of queueing delays counts with logarithmic (base 10) binning

Results show that queueing and charging delays have very little uncertainty. A small subset of OD-pairs exhibit queueing delay halfwidths in the bin $0.01h > h > 0.001h$ (36s-3.6s), which contains 111 ($n_{MC} = 500{,}000$) and 65 ($n_{MC} = 1{,}000{,}000$) OD-pairs, respectively. Given the size of the queueing halfwidth interval relative to travel delays durations, the queueing delay halfwidth is sufficiently small for both n_{MC}-values.

Similarly, there are 212 ($n_{MC} = 500{,}000$) and 77 ($n_{MC} = 1{,}000{,}000$) OD-pairs, respectively, with relative halfwidth >1% of the mean charging delays. The maximum relative halfwidth values are 0.0396 and 0.0207, respectively. Both results are accepted as sufficiently stable. However, the doubling of n_{MC} yields a disproportionate improvement to larger $\frac{h}{\overline{c_c}}$ −values. Therefore, $n_{MC} = 1{,}000{,}000$ is chosen.

A3.2.2. Delay Sensitivity to Charging Station utilization

In this section the sensitivity of charging and queueing delay results provided by the Monte Carlo simulation at a given number of iterations n_{MC} are investigated. To collect appropriate data, the Monte Carlo simulation is executed 10 times for the parameter set:

$$\{\alpha^r = 1.5, \beta^r = 1.0, \gamma^r = 0.09\}_{\forall r \in N},$$
$$\eta = 2.0, \qquad u = 0.2175, \qquad disrupted = true,$$

where the EV penetration γ is increased to yield a larger spread of link utilizations. The results are aggregated by charging station locations and the corresponding two-tailed 95% confidence intervals are calculated for each to investigate the relationship between utilization and the uncertainty of delays.

Results show that the confidence intervals of charging and queueing delays are subject to the composition of charging station locations. Uncertainty in each performance metric increases with heterogeneity and small overall capacity (number of EVSE). Fig. A-5 shows the two-tailed halfwidth of charging delays at charging station locations at 95% confidence plotted against their utilization.

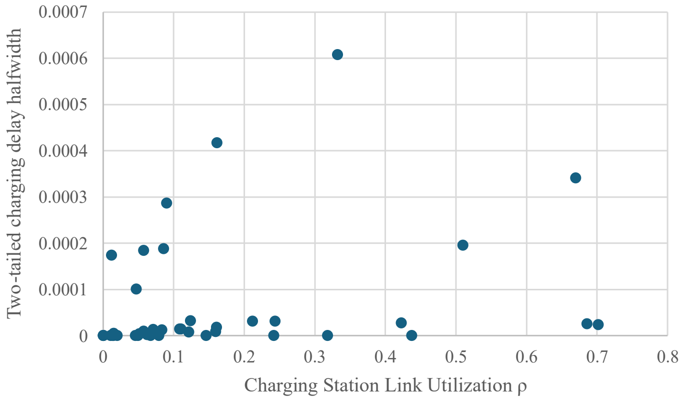

Figure A-5 Correlation between utilization and two-tailed charging delay halfwidth at 95% confidence

The figure shows that the confidence intervals of charging delays grow at different rates with increasing utilization. The charging station locations can be classified into ones with homogeneous and heterogenous EVSE. Every charging station location with a halfwidth >0.0001h has heterogenous EVSE. The only heterogenous charging station locations with halfwidths <0.0001h exhibit comparatively small utilizations ($\rho_{\tilde{a}} < 0.22$) while having large numbers of L3 EVSE assigned to them. This finding characterizes the uncertainty introduced by boundary operational regimes at charging station locations, as sampled EVs may be assigned to L2 or L3 EVSE. The outlier locations with larger utilizations enable small halfwidths by servicing most of the demand through the larger number of L3 EVSE. Conversely, even high utilization charging stations ($\rho_{\tilde{a}} \approx 0.7$) exhibit low uncertainties in charging delays, since they are comprised of only homogeneous EVSE. Nevertheless, charging delay uncertainty remains very small, as demonstrated by the maximum relative halfwidth of 0.00064.

Fig A-6 shows the two-tailed halfwidth of charging delays at charging station locations at 95% confidence plotted against their utilization.

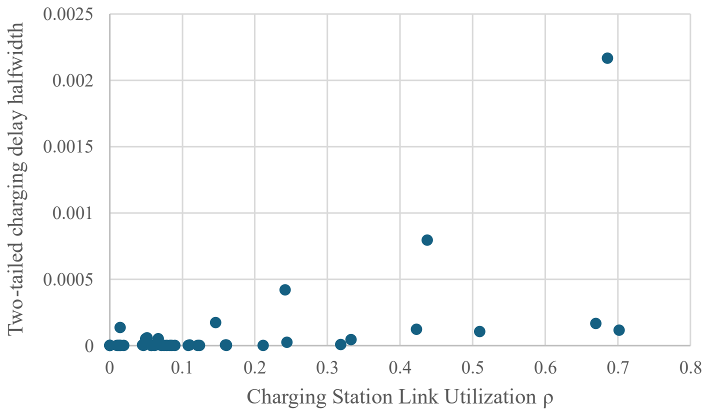

Figure A-6 Correlation between utilization and two-tailed queueing delay halfwidth at 95% confidence

The figure shows that, generally, queueing delay uncertainty increases with utilization. This is consistent with queueing theory, as queueing delays become more sensitive to stochastic noise with $\rho \to 1$. However, the rate constant with which the uncertainty increases with utilization differs. Similar to the charging delays, this rate is determined by the number and type of EVSE assigned to a location. The three charging stations locations with a halfwidths >0.0004h are comprised of two L2, two L2 and four L2 EVSE, respectively. Conversely, the low uncertainty locations with $\rho_{\tilde{a}} \approx 0.7$ have 12 and 15 EVSE assigned to them, respectively, providing a higher likelihood of every EVSE being occupied for a prolonged period.

A3.3. Sensitivity Analysis

A3.3.1. EV ownership

A sensitivity analysis of the TAP results was conducted for a parameter sweep of the global EV ownership rate γ. For the analysis all parameters were kept constant and the TAP was solved for $\gamma = \{0.0452, 0.06, 0.07,0.08,0.09\}$.

To investigate if the equilibrium flow results are stable with increasing EV ownership and consistent with expectations, the absolute change in the utilization of each charging station, $\Delta\rho_{\tilde{a}}$, is computed for each parameter values. The results for $\gamma \in [0.06, 0.09]$ are plotted against $\Delta\rho_{\tilde{a}}$ at $\gamma = 0.0452$ on a scatter plot and shown in Fig. A-7.

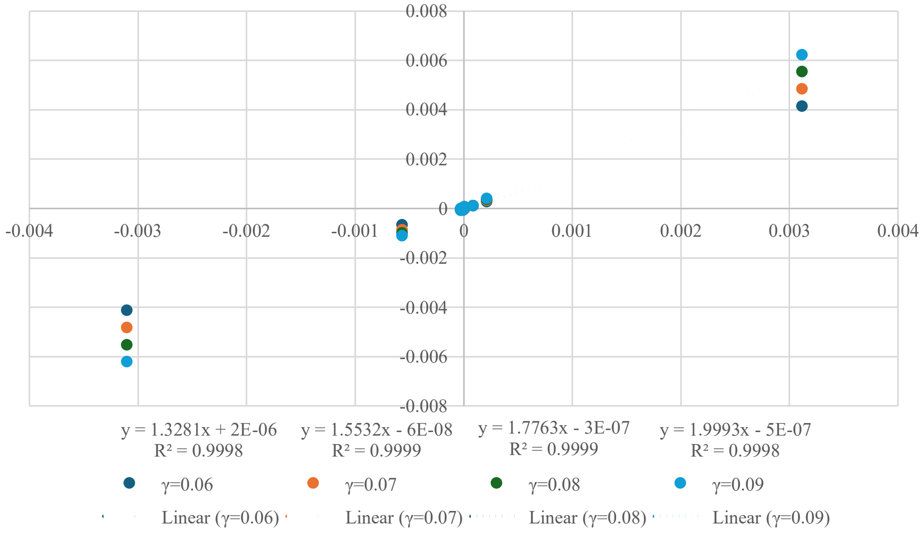

Figure A-7 Absolute utilization change of charging station locations for $\gamma \in [0.06, 0.09]$ against $\gamma = 0.0452$

The relationship between the results for the parameter sweep exhibit high linear agreement ($R^2 > 0.999$), indicating that the spatial redistribution of charging demand is largely invariant across γ, besides a linear scaling. Additionally, the $\Delta\rho_{\tilde{a}}$ increases monotonically with γ. Notably, the increase in $\Delta\rho_{\tilde{a}}$, which is shown in the graph's slope of the linear regression, very closely matches the increase of EV penetration relative to the default of $\gamma = 0.0452$.

This linear increase in charging station locations with γ is separately confirmed through the heatmap shown in Fig. A-8, displaying the utilization charging station locations (at baseline) across the parameter sweep.

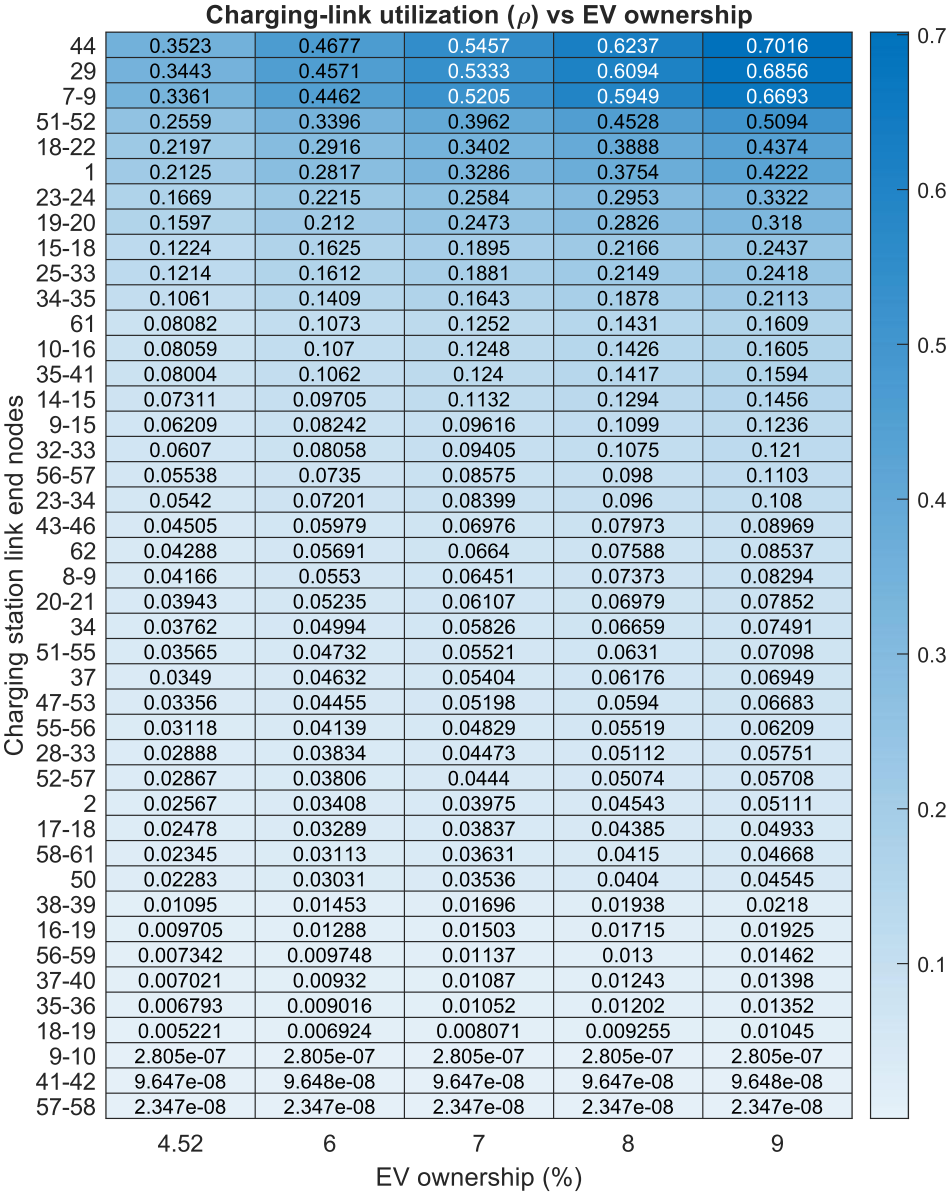

Charging station link end nodes	4.52	6	7	8	9
44	0.3523	0.4677	0.5457	0.6237	0.7016
29	0.3443	0.4571	0.5333	0.6094	0.6856
7-9	0.3361	0.4462	0.5205	0.5949	0.6693
51-52	0.2559	0.3396	0.3962	0.4528	0.5094
18-22	0.2197	0.2916	0.3402	0.3888	0.4374
1	0.2125	0.2817	0.3286	0.3754	0.4222
23-24	0.1669	0.2215	0.2584	0.2953	0.3322
19-20	0.1597	0.212	0.2473	0.2826	0.318
15-18	0.1224	0.1625	0.1895	0.2166	0.2437
25-33	0.1214	0.1612	0.1881	0.2149	0.2418
34-35	0.1061	0.1409	0.1643	0.1878	0.2113
61	0.08082	0.1073	0.1252	0.1431	0.1609
10-16	0.08059	0.107	0.1248	0.1426	0.1605
35-41	0.08004	0.1062	0.124	0.1417	0.1594
14-15	0.07311	0.09705	0.1132	0.1294	0.1456
9-15	0.06209	0.08242	0.09616	0.1099	0.1236
32-33	0.0607	0.08058	0.09405	0.1075	0.121
56-57	0.05538	0.0735	0.08575	0.098	0.1103
23-34	0.0542	0.07201	0.08399	0.096	0.108
43-46	0.04505	0.05979	0.06976	0.07973	0.08969
62	0.04288	0.05691	0.0664	0.07588	0.08537
8-9	0.04166	0.0553	0.06451	0.07373	0.08294
20-21	0.03943	0.05235	0.06107	0.06979	0.07852
34	0.03762	0.04994	0.05826	0.06659	0.07491
51-55	0.03565	0.04732	0.05521	0.0631	0.07098
37	0.0349	0.04632	0.05404	0.06176	0.06949
47-53	0.03356	0.04455	0.05198	0.0594	0.06683
55-56	0.03118	0.04139	0.04829	0.05519	0.06209
28-33	0.02888	0.03834	0.04473	0.05112	0.05751
52-57	0.02867	0.03806	0.0444	0.05074	0.05708
2	0.02567	0.03408	0.03975	0.04543	0.05111
17-18	0.02478	0.03289	0.03837	0.04385	0.04933
58-61	0.02345	0.03113	0.03631	0.0415	0.04668
50	0.02283	0.03031	0.03536	0.0404	0.04545
38-39	0.01095	0.01453	0.01696	0.01938	0.0218
16-19	0.009705	0.01288	0.01503	0.01715	0.01925
56-59	0.007342	0.009748	0.01137	0.013	0.01462
37-40	0.007021	0.00932	0.01087	0.01243	0.01398
35-36	0.006793	0.009016	0.01052	0.01202	0.01352
18-19	0.005221	0.006924	0.008071	0.009255	0.01045
9-10	2.805e-07	2.805e-07	2.805e-07	2.805e-07	2.805e-07
41-42	9.647e-08	9.648e-08	9.647e-08	9.647e-08	9.648e-08
57-58	2.347e-08	2.347e-08	2.347e-08	2.347e-08	2.347e-08

Figure A-8 Charging station link utilization progression with γ

These results are consistent with a monotonous increase in charging demand driven by the increase in EV ownership. Notably, the stability of the redistribution patterns is consistent with the small travel demand of recharging EVs, so that feedback between redistributed flows and emergent congestion delays is limited.

A3.3.2. VOT parameter

A sensitivity analysis of the TAP results was conducted for a parameter sweep of the value-of-time (VOT) constant η. For the analysis all parameters were kept constant and the TAP was solved for $\eta = \{1.5, 2.0,2.5\}$. The interval of $\eta = [1.5, 2.5]$ is chosen, as it represents the typical region for parameterizing the VOT of waiting relative to driving in literature [60].

Because η characterizes population-based user preferences, it is associated with a high-degree of uncertainty. Therefore, the sensitivity analysis seeks to investigate the sensitivity of resilience results against changing values of η.

Fig. A-9 shows a histogram of the relative error ε_{rel} in resilience measurements between for each OD-pair between $\eta = \{1.5, 2.5\}$ relative to the default value of $\eta = 2.0$, with

$$\varepsilon_{rel}^{rs} = \left|\frac{R_{trip}^{rs}(\eta) - R_{trip}^{rs}(\eta = 2.0)}{R_{trip}^{rs}(\eta = 2.0)}\right|.$$

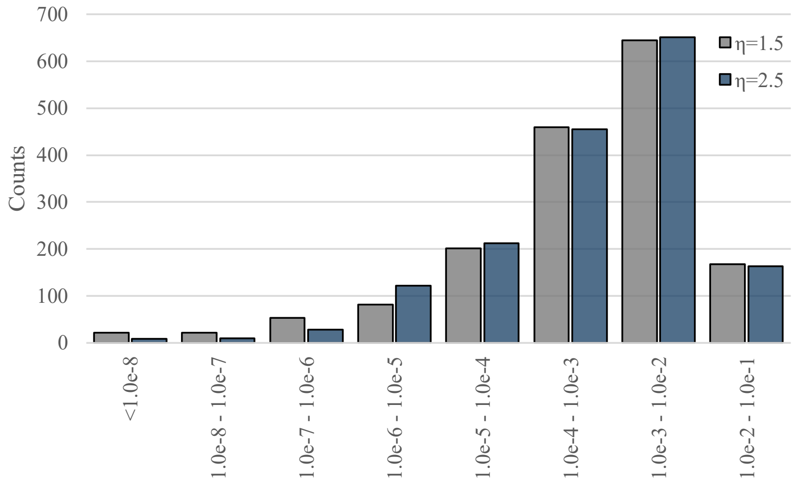

Figure A-9 Relative Error counts between $\eta = \{1.5, 2.5\}$ *and* $\eta = 2.0$

The figure shows that the relative errors of resilience values for OD-pairs are largely <1%. 167 OD-pairs for $\eta = 1.5$ and 164 OD-pairs for $\eta = 2.5$ exhibit relative errors >1%, with a maxima of 6.8% and 8.6%, respectively. These maxima represent outliers, as the mean relative error for both η-values shows 0.00348 with standard deviations of 0.00604 ($\eta = 1.5$) and 0.00647 ($\eta = 2.5$), respectively.

The relative errors appear to be stochastically distributed across the full set of OD-pairs, thereby not affecting the conclusions drawn from the case study. Table A-3 confirms this, as it shows the set of summary statistics previously used in Section 6.3 to characterize the network-level and tail-resilience performance of the case study.

Table A-3 Summary statistics comparing resilience results of different VOT-parameters

Statistic	$\boldsymbol{\eta = 1.5}$	$\boldsymbol{\eta = 2.0}$	$\boldsymbol{\eta = 2.5}$
Mean $\boldsymbol{R_{trip}}$	0.996	0.996	0.996
Median $\boldsymbol{R_{trip}}$	1.00	1.00	1.00
4th Percentile $\boldsymbol{R_{trip}}$	0.976	0.978	0.977
$\boldsymbol{N(R_{trip}^{rs} \leq 0.9)}$	12	12	12

These findings show that within the tested range of η the resilience results of the case study are largely insensitive to changes in the VOT-parameter. Summary statistics remain largely unchanged and the majority of OD-pairs show changes <1%.